Design and Synthesis of Three-Dimensional Interconnected Porous Carbon Nanostructure and Its Nanocomposite as Anodes for Li-ion Batteries

by

Yu Pei

A thesis

presented to the University of Waterloo

in fulfillment of the

thesis requirement for the degree of

Master of Applied Science

in

Chemical Engineering

Waterloo, Ontario, Canada, 2018

Author's Declaration

I hereby declare that I am the sole author of this thesis. This is a true copy of the thesis, including any required final revisions, as accepted by my examiners.

I understand that my thesis may be made electronically available to the public.

Abstract

With ever-increasing fossil fuel consumption and the resulting environmental problems, clean and sustainable energy fuel (such as hydrogen) or energy storage technologies are highly desirable. Rechargeable lithium ion batteries (LIBs) have been one of the most promising energy storage devices owing to their high energy density, no memory effect, and long cycle life. However, their low high-rate capability and limited specific capacity limit their high-energy application such as in electric vehicles (EVs).

Improving the energy density of LIBs requires anode materials with higher capacity and faster lithium ion diffusion capability. Carbonaceous materials, especially graphite, have been widely employed as the anode for LIBs. However, their capacity is reaching the theoretical capacity (372 mAh/g) based on the formation of LiC_6. Thus, high-capacity anode materials are urgently needed. Tin oxide is a potential anode material owing to its high theoretical specific capacity (783 mAh/g) and has been widely studied in recent years. Unfortunately, this material usually suffers from large volume changes upon lithiation and delithiation, leading to fast capacity decay and poor cycling performance.

To address these challenges, this thesis focuses on the engineering and construction of three-dimensional (3D) interconnected-nanoarchitecture advanced carbon materials and tin oxide/carbon nanocomposites. The first part is to design and fabricate 3D interconnected porous carbons. Two different carbon structures are developed: bulk amorphous carbon, which is pyrolyzed through a simple and convenient one-step calcination; and carbon networks, which are developed by using silica as a template. The carbon networks possess a unique three-dimensional structure and a large surface area with promising rate capability. Both carbon materials exhibit ultra-long durability, up to 2000 cycles, without significant capacity fade.

The second part of this work is the design and fabrication of 3D interconnected tin oxide/carbon nanocomposites. The tin oxide particles were deposited on both carbon spherules and carbon networks. Tin oxide has a high theoretical capacity, but it also suffers from severe capacity decay due to the large volume change and pulverization during the lithium insertion. Combining the tin oxide with porous carbon, buffer the volume expansion thus enhancing the battery life as well. The SnO_2/carbon network possesses an excellent cycling performance and can deliver a capacity of 673.1 mAh/g at 50 mA/g, and after 500 cycles, 210.74 mAh/g at 1000 mA/g with a capacity retention of 95.5%.

Keywords: lithium ion battery, 3D nanostructure, carbon networks, SnO_2/C.

Acknowledgements

The work reported herein was financially supported by the University of Waterloo.

The author would like to thank Dr. Zhongwei Chen and Dr. Aiping Yu for their meticulous guidance and tremendous assistance in the Master's study. Special thanks to Dr. Yuanli Ding, Dr. Ge Li, Dr. Wenwen Liu, and Sahar Hemmati for working closely with me and providing me with direction and support.

Many thanks go to the author's colleagues including Justin Raimbault, Zhiyu (James) Mao, Fathy Hassan, Zhong Ma, Pan Xu, Hao Liu, Dan Luo, Moon Park, Gaopeng Jian, Jingde Li, Jianbing Zhu, Guihua Liu, Xiaogang Fu, Rasim Batmaz, Yan Liu, Tongwen Yu, Jing Fu, Gregory Lui, Zhenyu Xing, Guobin Wen, Jie Ying, Zhichang Xiao, Rui Lin Liang, Archisman Ray, Ya-Ping Deng, Yining Zhang, Matthew Li, Yi Jiang, Lei Han, Abel Sy, and many other colleagues for their selfless help.

I would also like to thank my parents for their consistent love and support for me.

Moreover, I would like to acknowledge support from my reviewers, including Professor Zhongwei Chen, Professor Ali Elkamel, and Professor Jeff Gostick.

Table of Contents

List of Figures

1. Introduction

Increasing fossil fuel consumption and the problems related to global warming have pushed the development of renewable energy to displace conventional fossil fuels and the progress of energy storage technologies to store generated fluctuant electricity. Among the rechargeable batteries, lithium ion batteries (LIBs), as a type of advanced rechargeable energy storage device, have been widely investigated in order to improve their electrochemical properties (capacity and energy density) for electric automotive application.

Due to their high specific capacity, outstanding cycling performance, and excellent columbic efficiency, LIBs dominated the battery market soon after their first commercialization in 1991. Since lithium's low atomic number and high electrode potential (-3.04 V versus the standard hydrogen electrode) that lead to high energy density, it was expected to meet the increasing demand for high performance batteries. At present, LIBs are universally employed in everyone's cellular phones, tablets, laptops, and even electric vehicles (EVs). Although EVs are expanding their domain in the automobile market, their energy density is significantly lower than that of conventional gasoline vehicles. Their long charging time is another practical disadvantage, preventing EV's widespread use. However, in contrast to other battery types, such as lead-acid and nickel cadmium batteries, LIBs do have a host of attractive superior characteristics, including high energy density and no "memory" effects, but significant amount of effort is still needed to reduce the cost and expand the short lifespan for the next generation of high capacity LIBs.

As lithium is the lightest metal (6.94 g/mol, 0.534 g/cm^3) and possesses a high electric potential, the lithium-ion battery system theoretically has the highest energy density. Figure

1 clearly shows the gravimetric energy density and volumetric energy density of different battery types. It is obvious that lithium batteries possess the highest energy density among the most popular batteries on the market.

The idea of the lithium battery was first proposed in the 1950s, with first prototype created in the 1970s by Whittingham, using a lithium metal as the anode and TiS_2 as the cathode. Due to the dendritic lithium growth, these primary batteries were soon replaced by the new generation of rechargeable lithium ion batteries. In the 1980s, Goodenough claimed that cobalt oxide could be used as a positive electrode for secondary batteries, and this material became the foundation of LIBs. LIBs were first commercialized by the Sony Cooperation in 1991 [1], those $C/LiCoO_2$ rocking-chair cell had a potential of 3.6 V and possessed a gravimetric energy density of 120-150 W•h/kg. This type of battery is found in most of the portable devices in today's market [2], even though problems persist in it.

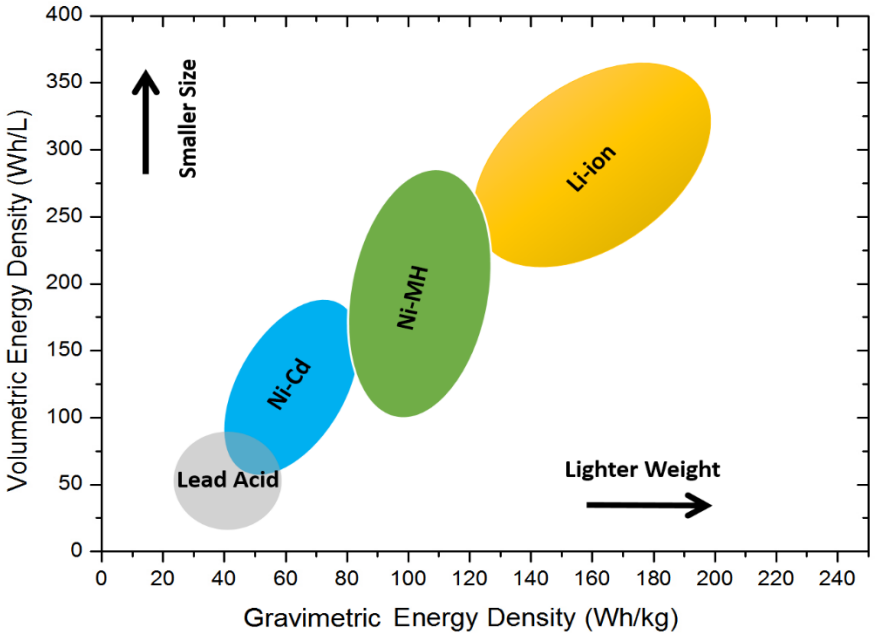

Figure 1. Diagram of the specific gravimetric energy density and volumetric energy density of various battery types.

1.1 Components and Working Principle of Lithium Ion Battery

A severe drawback of LIBs is the inhomogeneous lithium plating, that occurs lithium dendrites grow on the anode surface, eventually penetrating the separator, which should separate the two electrodes. The resulting connection causing a short circuit and thermal runaway of the battery [3]. To address this severe safety issue, the concept of the "rocking-chair" was proposed in the 1990s. At present, the rocking-chair charge and discharge mechanism is being used in all LIBs. While the battery is charging, lithium ions are extracted from the cathode and intercalate into the anode, and current flows from the anode to cathode [4]. Conversely, during the discharge, lithium ions deintercalate from the anode, diffuse through the electrolyte and then intercalate into the cathode. A rough schematic of a lithium ion battery charging/discharging is shown in Figure 2.

In a typical LIB (e.g., anode = graphite), the reactions on the two electrodes are as follows:

Cathode: $LiMO_2 \leftrightarrow Li_{1-x}MO_2 + x\ Li^+ + x\ e^-$ (1)

Anode: $x\ Li^+ + x\ e^- + 6\ C \leftrightarrow Li_xC_6$ (2)

During charge/discharge, lithium ions transfer between the anode and cathode via an ionic conducting electrolyte. Usually, the electrolyte is composed of lithium hexafluorophosphate ($LiPF_6$) in a mixture of ethylene carbonate (EC), dimethyl carbonate (DMC), and diethyl carbonate (DEC). This mixture is suitable for LIBs and is widely used.

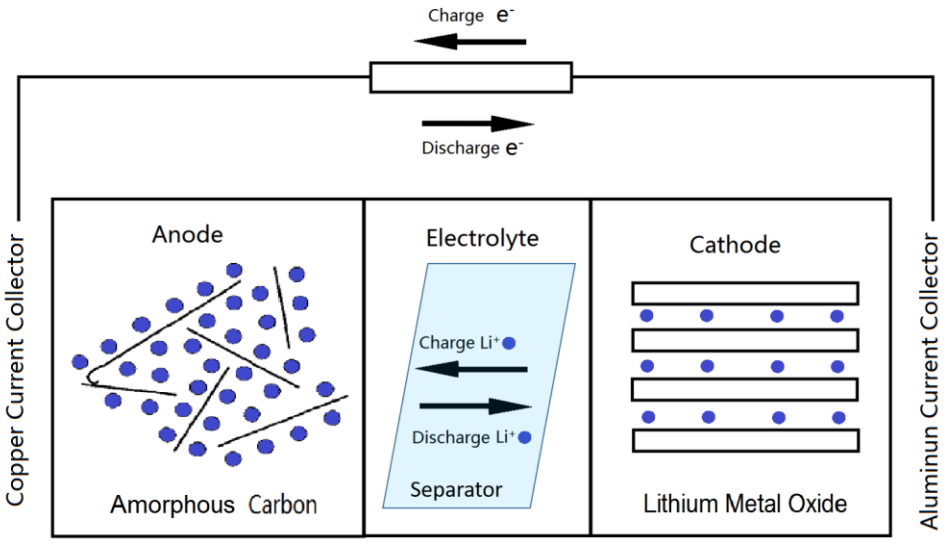

Figure 2. Schematic of lithium ion battery.

1.2 Current Status and Challenges of Lithium Ion Batteries

Conventional LIBs are comprised of carbonaceous anodes, and cathodes consist of intercalation compounds. Usually, the carbonaceous anodes are graphite, hard carbon, and soft carbon. The cathodes are made from $LiMO_2$ (M = Co, Ni, Mn), Li[Co, Ni, Mn]O_2, $LiMPO_4$ (M = Fe, V, Co, Ni, Mn, Cu), $LiMn_2O_4$, or V_2O_5.

Current LIBs have many advantages over other types of batteries and possess a high gravimetric energy density as they have high electrode potential (3.6 V) with a good capacity. They can achieve a gravimetric energy density of 140 W•h/kg and volumetric energy density of around 300 W•h/L, while Cd-Ni batteries and MH-Ni batteries have only half of that (Cd-Ni: 40 W•h/kg and 125 W•h/L; MH-Ni: 60 W•h/kg and 165 W•h/L). Furthermore, LIBs have a long lifespan, high energy efficiency, and good high-rate capability without memory effect.

Despite these strengths, LIBs are facing challenges as well. The high internal resistance and low electrical conductivity can be the results of using organic electrolytes. In addition, the high cost of electrodes, limited capacity, and capacity decay issues are hindering their application in EVs, and protection circuitries are required for safety.

To develop high performance LIBs, their active materials should fulfill the requirements of reversible capacity, good ionic and electrical conductivity, long cycle life, high lithium diffusion speed, and low cost [5]. However, the most important index for evaluating an LIB's performance is its energy density and lifespan.

Marom *et al*. [6] suggested a road map for the direction of LIB research, shown in Figure 3. One of the main limits of the state of the art for LIBs is the capacity limitation of the anode material. At present, graphite is widely used as the anode of commercial LIBs owing to its low volume expansion during charge and discharge, but the lithium insertion capacity of this material (372 mAh/g) is relatively low. For the new applications in EVs and large scale electrical storage systems, new generations of negative electrode materials are essential to advance the energy density and cycle life [7]. Recently, significant work has focused on improving the anode active materials in terms of capacity, battery lifetime and energy/power density.

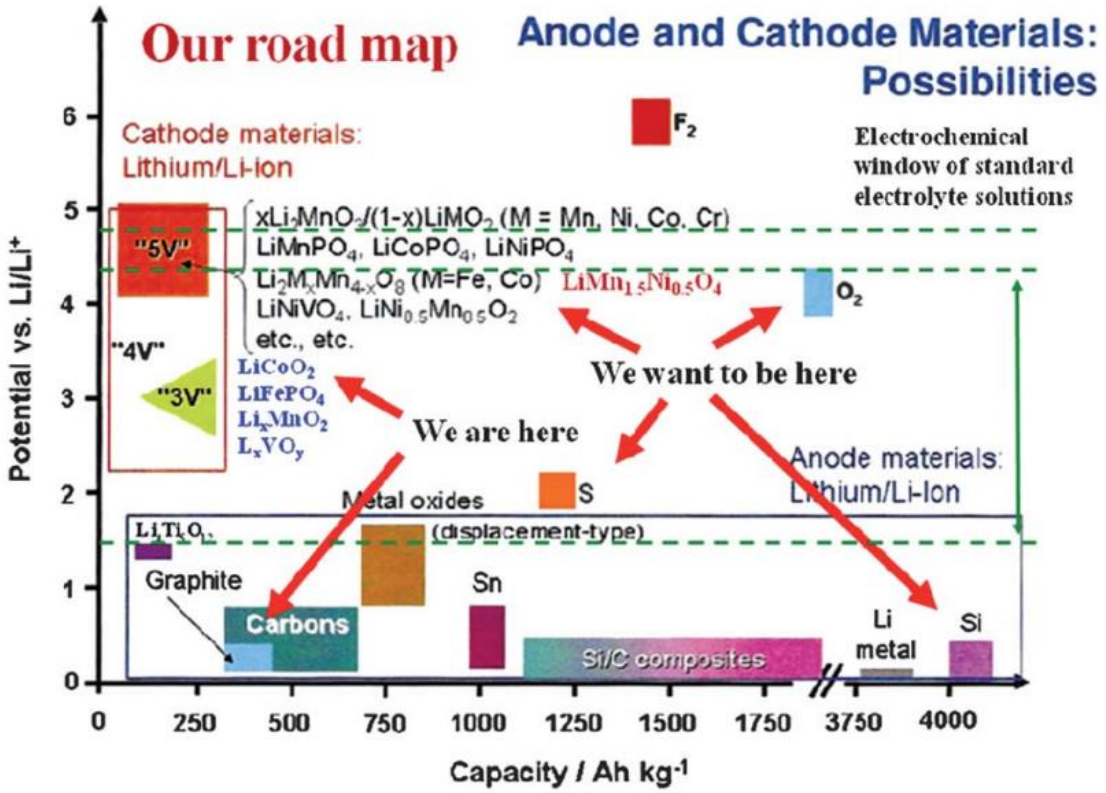

Figure 3. The road map for the direction of LIBs [6].

1.3 Cathode

As one of the essential components in lithium ion batteries, the cathode is responsible for providing lithium ions for lithiation when the anode material is empty (not pre-intercalated with lithium ions). The discharge capacities of the current widely used cathode materials, such as $LiCoO_2$, $LiFePO_4$, and $LiMn_2O_4$ are lower than 200 mAh/g [8]. In order to improve the state of the art of LIBs, the requirements specifically related to cathode materials are as follows:

i) Lithium ions should have a high redox potential in the lithium intercalation

compounds to obtain a stable output voltage;

ii) The active material should have sufficient space for abundant lithium ions to intercalate and deintercalate;

iii) The structure of the cathode material should be stable during charge and discharge to achieve a good cycling performance;

iv) The ionic and electric conductivity of the active material should be high to reduce the polarization and to allow the battery to charge/discharge at high current;

v) The cathode material should be stable and unlikely to react with electrolyte.

So far, the lithium intercalation compound $LiCoO_2$ has been widely employed as the positive electrode in commercial LIBs. IN addition to its high output, a theoretical capacity of 273 mAh/g, but only 130-140 mAh/g can in practice be reversibly deintercalated. Considerable work has been done regarding next generation cathode materials.

Some transition metal cations, including Ni, Co and Mn were reported to have good performance as cathode materials, which can be attributed to the intercalation and deintercalation of lithium ions in the host structure of transition metals. Layered $LiNiO_2$, which has a similar structure to $LiCoO_2$, was first considered by J. R. Dahn *et al*. [9]. This material has a theoretical capacity of 275 mAh/g, and can achieve a reversible capacity of 190-210 mAh/g. Although $LiNiO_2$ is cheaper and has higher capacity than $LiCoO_2$, it is still hard to commercialize owing to its poor structural stability and fast capacity decay during cycling [10]. A ZrO_2-coated $LiNiO_2$ cathode material was found to be more structurally stable and electrochemically reversible [11]. Kim and Chuang reported that a layered $Li[Co, Ni, Mn]O_2$ with a high capacity of 160 mAh/g and milder thermal behavior was achieved with relatively low cost [12].

Olivine $LiMPO_4$ (M = Fe, V, Co, Ni, Mn, and Cu) materials were investigated as cathode active materials for LIBs, where different elements have various specific capacities. Okada *et al*. reported that $LiCoPO_4$ exhibited a 4.8 V discharge plateau of 100 mAh/g and that the capacity of $LiFePO_4$ is 160 mAh/g at 3 V [13]. Martha *et al*. found that $LiMn_{0.8}Fe_{0.2}PO_4$ carbon-coated nanoparticles possessed a reversible capacity of 165 mAh/g along with good cycling performance and rate capabilities [14].

Recently, vanadium oxides have attracted much attention owing to their high-energy density, convenient fabrication and low cost. As one of the most promising cathodes among the vanadium oxides, V_2O_5 possesses a high theoretical capacity of 294 mAh/g or 442 mAh/g corresponding to different reactions [8]. The latest research of Ji Wu *et al*. has reported that a V_2O_5 asymmetric membrane cathode can achieve a capacity of 160 mAh/g at a current density of 100 mA/g with a good cyclic performance [15]. To further improve the capacity of V_2O_5, various morphologies have been investigated. Vanadium oxide nanofibers [16], nanotubes [17], nanorods [18], and nanobelts [19] can achieve 300-400 mAh/g [20].

1.4 Anode

1.4.1 Carbon-based Anodes

Regarding the anodes, carbon materials are currently dominating the LIB market. According to the carbon structure, the carbonaceous material can be roughly classified into two types: graphitic carbons (graphite and graphene) and amorphous carbons (soft carbon and hard carbon).

Graphitic carbon

Among the carbonaceous anodes, graphite is the most used material [6], can provide a capacity of 372 mAh/g, and possesses a high electric conductivity. As shown in Figure 4, the highly ordered graphitic carbon is composed of graphene layers. In graphite, only one layer of lithium can be intercalated for each graphene layer. The d-spacing value of graphite is 0.335 nm. During the lithium insertion, the d_{002} spacing will extend to 0.372 nm and shrink back to 0.335 nm after the lithium deintercalation [21]. The structural stability and battery lifetime are affected by the volume change during cycling. Furthermore, the lithium ions can only intercalate into the edges of the graphene stacks due to the highly ordered carbon structure. This issue can reduce the Li^+ transport rates and the reversible capacity of graphite anodes. A typical graphite anode has an obvious plateau in its potential profile.

Recent research on anode materials has focused on graphene, a one-atom-thick 2D carbon sheet, owing to its high surface area, high electric conductivity, and excellent flexibility. Graphene anodes can achieve a high reversible capacity up to 1264 mAh/g at a low current density of 100 mA/g [22]. However, graphene nanosheets have a severe aggregation issue. Zhou *et al*. developed a graphene nanosheet/Fe_3O_4 composite to improve the cyclic stability with a high reversible capacity of 1026 mAh/g at a low current density of 35 mA/g [23].

Amorphous Carbon

Amorphous carbon is a type of highly disordered carbon with abundant defects in its structure. Based on the characteristic of being graphitizable or non-graphitizable under high temperature, amorphous carbon can be further classified into soft carbon or hard carbon. The lattice structures of amorphous carbons are shown in Figure 4.

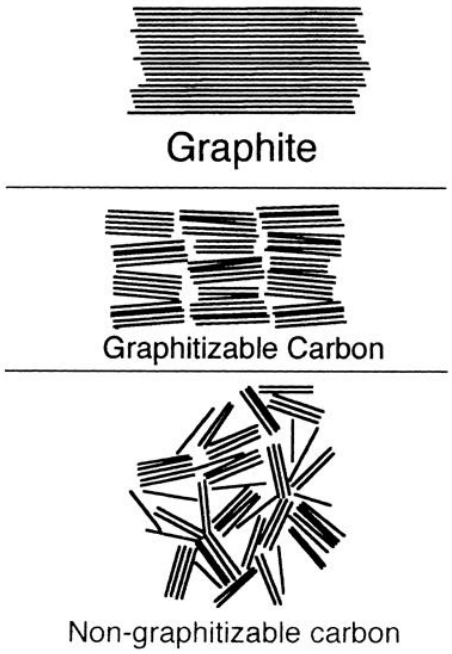

Figure 4. Schematic illustration of: graphite, graphitizable carbon (soft carbon), and non-graphitizable (hard carbon) [21].

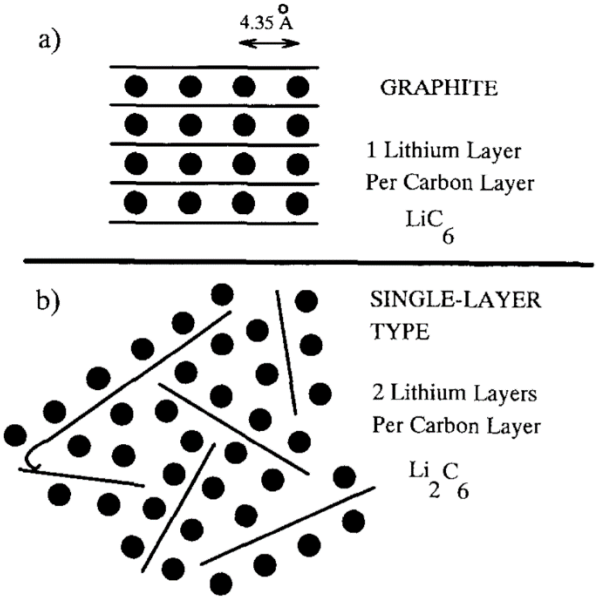

Figure 5. Schematic diagram showing the intercalation of lithium in (a) graphite and (b) a

single-layer hard carbon [24].

Soft carbon such as coke generally contains C-H bonding and is also named hydrogen-containing carbon. It can be graphitized by high temperature heat treatment, and has a d_{002} spacing in the range of 0.335-0.372 nm [21]. Although this carbonaceous material has a high capacity, it suffers from overvoltage and voltage loss [25–27]. Soft carbon was used as an anode in the first LIB in 1991. Due to fast capacity fading, the coke anode was replaced by other carbon materials. Therefore, soft carbon is not suitable for LIB applications.

Non-graphitizable carbon is also known as hard carbon, which contains much less C-H bonding than soft carbon, and has been widely investigated. Hard carbon is usually pyrolyzed from sucrose [28], glucose [29], cellulose [30], phenolic resin [31], etc. In contrast to soft carbon, hard carbon is non-graphitizable, and its d_{002} spacing is broader than 0.372 nm, which makes lithium insertion and extraction easier. In addition, compared to graphite, hard carbon possesses a better cyclic performance and higher reversible Li^+ storage capacity. In 1995, Zheng *et al*. [26] and J.R. Dahn *et al*. [24,32] proposed the "house of cards" structural model of hard carbon (shown in Figure 4 and Figure 5 (b)). According to their theory, single carbon sheets are stacked like a "house of cards", where the graphene layers randomly oriented. Both amorphous and graphitized structures exist in hard carbon. During the intercalation process, lithium ions are first inserted into the graphitized part and then intercalated into the amorphous part [33]. It is believed that the lithium ions could be adsorbed on both surfaces of the small graphene sheets, leading to two layers of Li^+ for each carbon sheet and providing extra lithium insertion capacity (maximum: Li_2C_6, 740 mAh/g) [24,32]. Furthermore, the enhanced capacity is also associated with the adsorption on the internal surfaces of nanopores formed by the carbon "cards" and voids in micro-cavities [24,27,32,34,35]. The porous structure also provides a large surface area to host extra lithium ions and provide a shorter Li^+ diffusion path [36–40]. However, porous hard carbon also has drawbacks:

for instance, low initial columbic efficiency (around 50%) due to the formation of solid electrolyte interface (SEI) films on its surface and low tap density that limits its volumetric energy density.

Initially, J.R. Dahn *et al.* investigated the influence of precursor, pyrolysis temperature, heating rate, gas flow rate, ball milling, acid wash, etc. on the electrochemical performance of disordered carbon anodes [24,28,41–43]. Ni *et al*. investigated a phenolic resin-derived hard carbon as the negative electrode for an LIB, and the anode delivered a capacity of 526 mAh/g in the first cycle with an initial columbic efficiency of 80% [31]. To reduce the irreversible capacity in the first cycle, hard carbon and microcrystalline graphite (MG) core-shell composite materials were investigated, and this material possesses a high initial columbic efficiency (up to 89.8%) and good cycling stability, but the reversible capacity is still lower than 300 mAh/g at 0.2 C [44].

Considering the low cost and sustainability of biomass as a carbon source, a number of studies have been done to investigate the performance of biomass-derived disordered carbons as anodes for LIB. Jiang *et al*. reported a bamboo-derived carbon fiber with surface defects and hydrogen functional groups as anodes for LIBs [45]. Memarzadeh *et al*. developed disordered carbons from banana peels for both sodium and lithium ion battery anodes [46]. Lv *et al*. investigated peanut shell derived hard carbon anodes with excellent cyclic stability [47].

The morphology of carbon has attracted significant attention as well. In the 2000s, Huang *et al*. proposed sugar-derived hard carbon spheres (HCS) obtained using a simple hydrothermal method and achieved a reversible capacity of 400-500 mAh/g with a good performance [35,48–50]. The emulsion polymerization process of dewatering sugar spherules that Huang *et al*. used in their work [49] is shown in Figure 6. Huo *et al*. reported mesoporous

nitrogen-doped carbon hollow spheres obtained by a mesoporous hollow silica sphere template with dopamine (shown in Figure 7) [51]. These hollow spheres achieved a high reversible capacity of 485.7 mAh/g after 1,100 cycles at a current density of 500 mA/g. However, the preparation methods for hollow spherical templates and carbon are sensitive and time consuming. In the same work, Huo *et al*. prepared nitrogen-free glucose-derived hollow carbon spheres and only got a capacity around 100 mAh/g at a current density of 500mA/g.

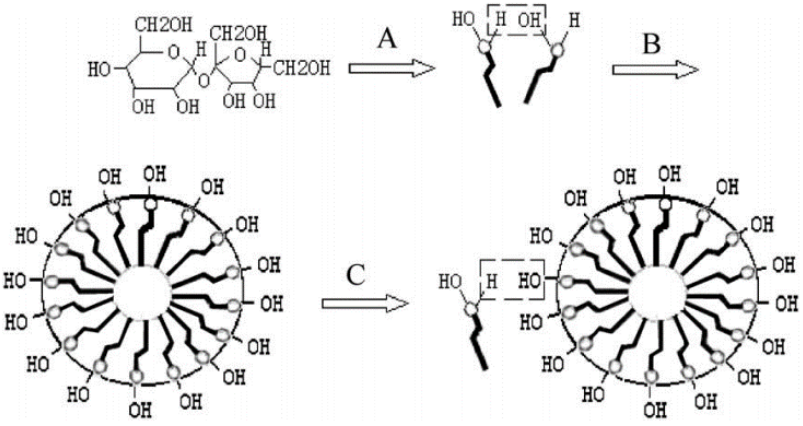

Figure 6. Schematic of the possible formation process of dewatering sugar spherules through emulsion polymerization. (A) Dewatering of sugar, (B) formation of spherical micelles, and (C) growth of the nuclei [49].

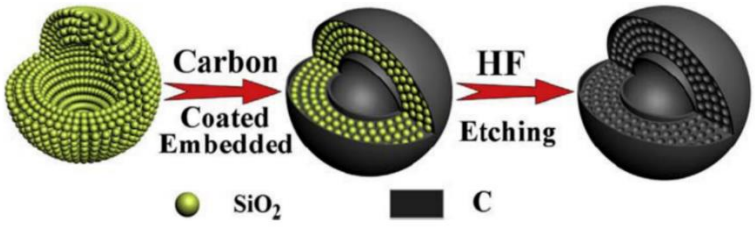

Figure 7. Schematic of the fabrication procedure for mesoporous nitrogen-doped carbon hollow spheres [51].

1.4.2 Tin Oxide-based Anodes

To meet the urgent demand for improving energy/power density and battery lifetime, transition metal oxides have been investigated as well. The group IV elements can provide high energy density at low costs. Among these elements, tin (Sn) and its oxide (SnO_2) have attracted much attention as they can offer high reversible theoretical lithium ion capacities, and exhibit low reactivity with electrolytes. Unfortunately, their large volume change during the charge/discharge process leads to electrodes' cracking and structural reconfiguration. Compared to tin, SnO_2 is believed to be more stable during the lithiation/delithiation process due to the formation of a Sn/Li_2O composite matrix before the formation of $Li_{4.4}Sn$ alloy during lithiation [52,53]. The Sn/Li_2O can buffer the expansion stresses and reinforce the structure.

However, the large volume expansion of more than 300% during lithiation still causes pulverization, capacity fading, and loss of electric conductivity. Furthermore, the formation of metallic Sn nanoparticles during lithiation can cause severe aggregation, leading to quick capacity decay [54].

To overcome the capacity decay caused by the volume expansion and constriction, various morphologies of tin oxide particles have been designed and fabricated. Meduri *et al*. reported on using hybrid tin oxide nanowires covered with tin nanoclusters as a high capacity anode, and this hybrid material achieved a good cycling performance [55]. The stability was attributed to spacing and high surface area that allowed volume expansion, and the existence of tin that allowed a reversible reaction. Mohamedi *et al*. investigated the electrochemical performance of amorphous tin oxide films and revealed the correlation

between the stability and the cut-off voltage. They claimed that the tin oxide could reform at a voltage higher than 1.5 V [53]. Hollow tin oxide spheres were pursued to alleviate the large volume expansion, but the capacity of this anode material faded quickly as well [56]. However, utilizing nanomaterials may not be a perfect solution, as nanoscale particles can cause severe aggregation problem and aggravate the capacity decay [57].

A tin oxide/carbon composite is proposed to enhance stability. In this composite, carbon serves as a physical buffer against for the large volume expansion. Lou synthesized double shelled SnO_2/carbon composite hollow spheres [58] and SnO_2/carbon hollow spheres [59], and showed that the capacity fade was alleviated. By considering a dense core-shell structured SnO_2/C anode, Liu and others demonstrated that the electrochemical performance of tin oxide/carbon composites increased in the following order: solid SnO_2 anode < hollow SnO_2 anode < traditional core-shell SnO_2/C anode < dense core-shell structured SnO_2/C anode [57]. Furthermore, carbon-encapsulated porous SnO_2 cubic anode [60], SnO_2 quantum dots/GO [61], and SnO_2-carbon-coated sepiolite nanofibers were reported recently [62].

1.5 Project Objectives

The development of current carbon-based anode materials are facing a bottleneck and cannot fulfill the increasing demands for lithium-ion batteries. Hard carbon and tin oxide are both potential anode materials. Hard carbon has an amorphous structure that can provide more capacity than graphite and a shorter lithium-ion diffusion path. On the other hand, although tin oxide has a promising reversible theoretical capacity (783 mAh/g), it suffers from large volume expansion and nanoparticle aggregation, which lead to capacity fading and poor rate capability.

To overcome the drawbacks of these two materials, the work of this thesis focuses on

a) the design and fabrication of hollow interconnected carbon shells with improved capacity;
b) the development of SnO_2/carbon composites with different morphologies to enhance durability and rate capability.

2. Characterization Methods

This chapter introduces the physical and electrochemical characterization methods that were used in this work, including scanning electron microscopy (SEM), transmission electron microscopy (TEM), X-ray diffraction (XRD), thermogravimetric analysis (TGA), Brunauer-Emmett-Teller Analysis (BET), Raman Spectroscopy, and lithium ion battery evaluation. The main purpose of using these physical characterizations is to reveal the information on the morphology, crystal structure, chemical composition as well as surface area. The electrochemical evaluation via coin-cell testing is used to investigate and understand the electrochemical performance of the obtained amorphous-carbon-based materials in the lithium ion battery as anodes.

2.1 Scanning Electron Microscopy (SEM)

Scanning electron microscopy (SEM) is one of the most versatile microscopy techniques available for analyzing the topological properties, structure and, chemical composition characteristics in the micro and nanoscale, with a focused high-energy electron beam scanning across the surface of the sample. Owing to the short wavelength of an electron beam and focusing by electromagnetic condenser lenses, SEM can obtain a perfect point source and better resolution to reveal fine surface structures of nanomaterials.

As shown in the Figure 8, SEM employs an electron gun to release electron beam as the illumination source and utilizes electromagnetic coils as condenser lenses. The high-energy electron beam is obtained by accelerating electrons with a potential drop voltage, which provides kinetic energy for the electrons. For conventional SEM, the accelerating voltage applied on electron guns is usually operated in a range from 1 to 30 kV.

Generally, electron guns can be classified into two categories: thermionic electron gun, which produces electrons by heating materials; and field emission gun (FEG), which applies a large electrical potential between a single crystal tungsten tip and two anodes. The first and the second anodes are used to extract electrons from the very fine tungsten tip and accelerating electron beam, respectively. Compared with the thermionic source electron gun, the FEG provides an enhanced electron brightness and a higher resolution. Nowadays, the FEG is customarily equipped on modern SEMs as the illumination source. There are numerous advantages to using electron beam, including small wavelength (λ), high resolution, and a finely focused probe. Furthermore, the energetic electrons can generate secondary signals (X-rays, photons), which reveal the chemical characteristics with further analysis.

A series of electromagnetic lenses is used to focus the spread beam. In essence, the electromagnetic lenses are coils of wires. While applying current on the coils, the path of the electron beam is simultaneously adjusted. Owing to the divergence of the electron beam after passing through the anode plates, it needs to be converged and collimated into a parallel beam by condenser lenses and an aperture. In addition, an objective lens with appropriate demagnification is utilized to focus the electron beam into a fine probe at the surface of the specimen.

More than one type of electron is generated when the energetic electrons strike the specimen surface, including secondary electrons, backscattered electrons, and auger electrons. Secondary electrons carry the topographic and morphologic information, which are created by the ionization of the specimen atoms at the surface of the specimen. Electrons that are elastically scattered during the deflection of the primary electron by the atomic nucleus of the specimen are called backscattered electrons (BSE). BSEs escape from a large region under the specimen's surface, and provide topographic and composition

information by yielding atomic number contrast. Auger electrons are ejected by absorbing the released energy in the deexcitation process, which is characteristic of the specimen atom. Therefore, the auger electrons are available for providing information related to specimen chemical composition in the top few atomic layers.

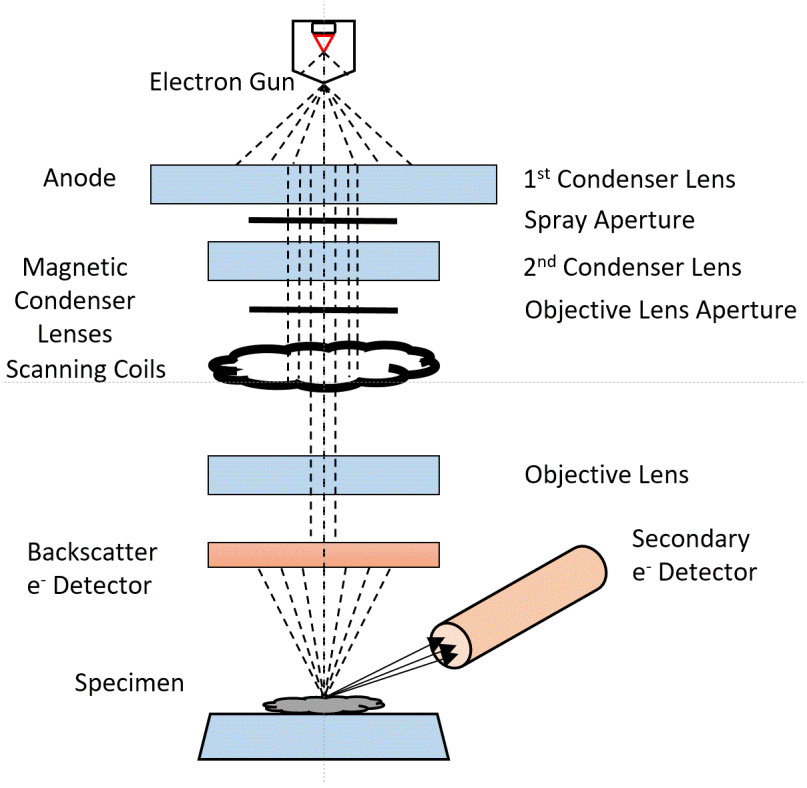

Figure 8. Schematic diagram of a scanning electron microscope (SEM).

2.2 Transmission Electron Microscopy (TEM)

Transmission electron microscopy (TEM) has been widely used in material research for direct visualization of the morphological and crystallographic information, such as crystal lattice and atomic defects with high resolution. High-resolution transmission electron microscopy (HRTEM) is an imaging mode of transmission electron microscopy. Due to

phase contrast, HRTEM exhibits a higher resolution.

The operating principle of TEM is the interaction between the electrons and the specimen. An electron beam is generated and accelerated by an electron gun, which is mentioned in the prior section (2.1 Scanning Electron Microscopy). After being focused by a series of electromagnetic lenses, the electron beam encounters the specimen and transmits through it. A magnified image is displayed on a fluorescent screen. In modern TEM instruments, digital camera are usually installed to record the obtained images, and application software is also available for analysis.

As Figure 9 indicates, the components of a modern TEM are classified into three parts from the top down. First, the illumination system (also known as condenser lens system) is composed of an electron gun and a condenser system. Following is the imaging system, including an objective aperture, objective lens, diffraction lens, intermediate aperture, intermediate lens, projective lenses, and the observation system for the image and diffraction pattern. Moreover, a vacuum system is also necessary in the TEM to obtain a coherent controlled e^- beam and to keep the chamber clean. Typically, the sample is 3 mm in diameter and less than 80 μm thick, prepared on a very thin Cu grid. While the incident electron beam is interacting with the specimen atoms, both elastic and inelastic scattering processes are simultaneously taking place.

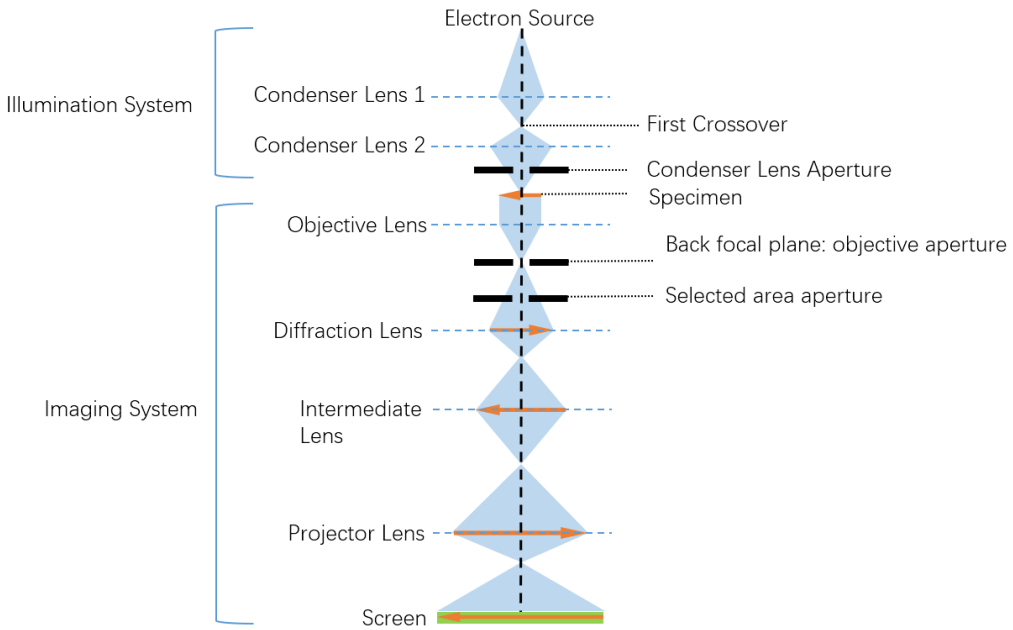

Figure 9. Experimental set-up of a transmission electron microscope (TEM).

TEM is available for imaging features and atomic structures of specimen's surface. In addition, the information of periodicity and orientation, crystal structures and lattice parameters, as well as the chemical composition can be obtained from the diffraction patterns of the convergent beam electron diffraction pattern (CBED), the crystal spot patterns of selected area electron diffraction (SAED), and the energy-loss spectrum of electron-energy-loss spectroscopy (EELS), respectively.

2.3 X-ray Diffraction (XRD)

X-ray diffraction (XRD) is a widely used as a chemical analysis method in crystallography, which can reveal the chemical component and crystalline structure information of samples. The basic operating principle is based on the interaction between the X-ray and the

sample's atoms. Typically, the X-ray source used in XRD is copper and molybdenum. The wavelength is in a range of 0.154 nm-0.08 nm, comparable to the diameter of sample's atoms. Therefore, the incident x-ray can penetrate into the bulk material and be diffracted by the sample at a specific incident angle. As Figure 10 below depicts, when the X-ray is irradiating with a changing incident angle, the diffraction at certain angles is detected. Herein, a lattice correlated interference pattern is generated with the information of both incident angle position and intensity.

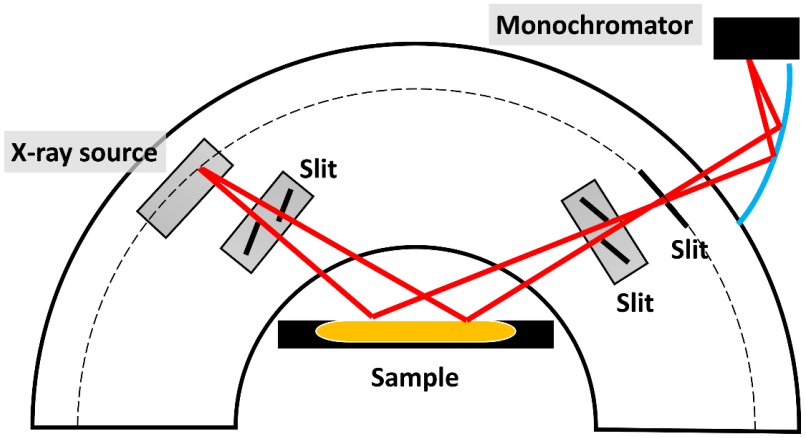

Figure 10. Schematic diagram of XRD layout.

The intensity of the patterns correspond to specific lattice planes. With the help of Bragg's law, the relationship between the X-ray incident angle and the lattice spacing is expressed with a brief equation:

$$2d\ sin\theta = n\lambda$$

d = lattice spacing

θ = X-ray incident angle (half value of peak position)

n = integer (diffraction peak's order)

λ = X-ray wavelength

(3) Bragg's Law

In addition, the XRD pattern contains the information of the size of crystals in solid powders. The size of crystal particles can be calculated from the Debye-Scherrer equation below:

$$\tau = \frac{K\lambda}{\beta \cos \theta}$$

τ = mean size of the crystalline

K = shape factor

λ = X-ray wavelength

β = line broadening at half the maximum intensity (FWHM)

(4) Debye-Scherrer Equation

2.4 Raman Spectroscopy

Raman spectroscopy is a vibrational spectroscopy technique, commonly utilized in chemistry for lattice structure analysis and molecule identification. The operating principal of Raman spectroscopy is based on the inelastic scattering of monochromatic light. When the sample is illuminated by a radiation source, the laser beam is scattered from specimen's molecules, and both elastic and a small fraction of inelastically scattering occurs. The electron is excited to a higher energy state in the scattering process, and when the Raman effect occurs, the energy decays to a lower level. The final level is even lower than its initial energy states. This is termed as inelastic scattering. Since some energy is transferred between specimen's molecules and photons, the energy and wavelength of the incident and scattered photons are not the same. The energy difference is denoted with the length of arrow in Figure 11 (a).

As depicted in Figure 11 (b), the Raman experimental set-up usually consists of five major components: a laser excitation source, a sample illumination system and light collection optics, a filter or spectrophotometer for wavelength selection, a detector that functions with a charge coupled device (CCD), a photo multiplier tube (PMT) or photodiode array, and a recording device. A sample is usually illuminated with a laser beam. The inelastic scattering light is collected by a lens and transferred through an emission filter or spectrophotometer. A Raman spectrum is subsequently generated after the detector collects signals.

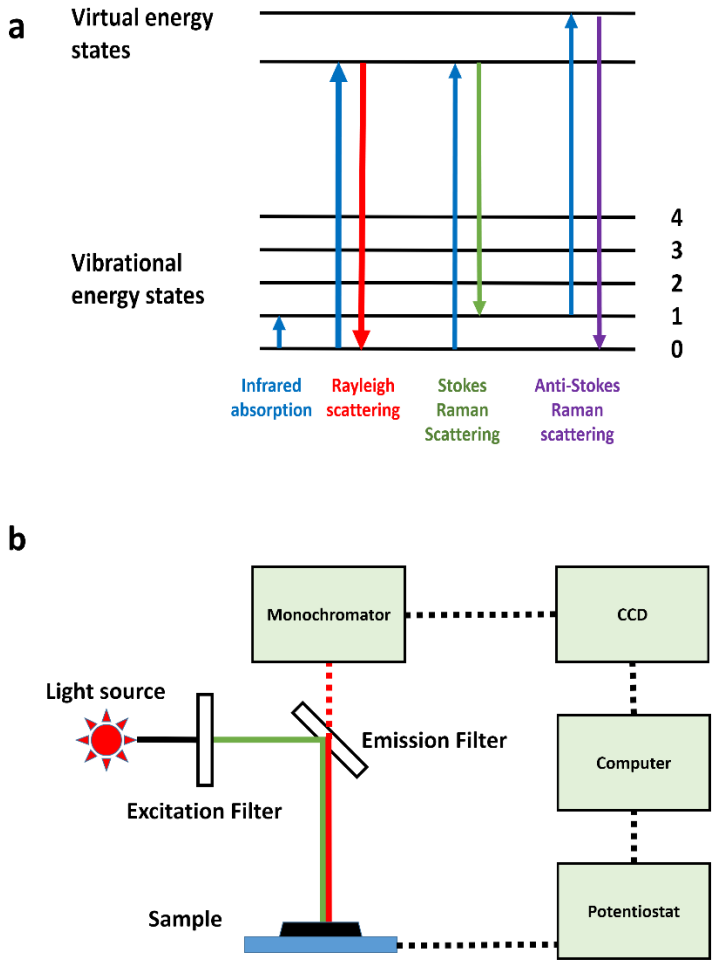

Figure 11. (a) Energy-level diagram, (b) experimental setup for spectroelectrochemical Raman experiments.

In addition, Raman spectroscopy technique has plenty of advantages. Raman can be used for both organic and inorganic chemicals, without damage to the sample, and with a short measurement time (only a few minutes).

2.5 Thermogravimetric Analysis (TGA)

Thermogravimetric analysis is a technique used to analyze the sample's weight change as a function of temperature or time. A TGA measurement is performed by heating the specimen in a controlled atmosphere (N_2, O_2, Ar, etc.), while the weight change is measured and recorded by a precision balance. As depicted in Figure 12, an inert heat resistant specimen holder supports the sample above a very accurate balance. The heating temperature, ramp rate, and rest time can be set with furnace's software.

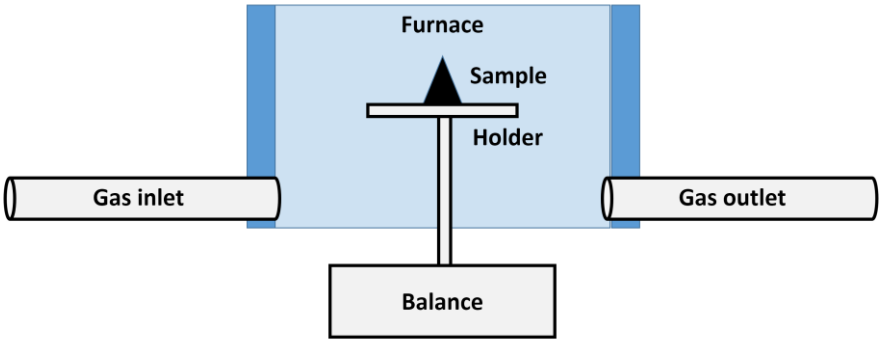

Figure 12. Schematic diagram of the set up for a TGA experiment.

The main purpose of this analytic method in the second subproject (4. Design and Fabrication of 3D Interconnected Porous Carbon Spheres Encapsuled Ultra-small SnO_2 Nanoparticles as Nanocomposite Anodes for LIBs) is to determine the exact content of tin oxide in the tin oxide/carbon composite. As all the carbon would turn into carbon oxide or

carbon monoxide in a gaseous state, if an air atmosphere is chosen, only tin oxide will be left behind.

2.6 Brunauer-Emmett-Teller Analysis (BET)

The Brunauer-Emmett-Teller (BET) analytical technique is widely used in measuring the surface area of nano/micro-materials. Typically, the BET analytical method is used to obtain a porous material's specific surface area, average pore-size, and pore-size distribution via adsorption of inert gas molecules on sample's surface. In this study, the carbon-based samples' specific surface area and pore-size distributions were obtained using the BET analysis technique.

The BET theory is based on the following three assumptions:

First, the material surface is homogeneous and the adsorption is equally distributed. Second, only monolayer adsorption occurs, without interaction between adsorbed layers. Finally, the number of adsorbed layers is infinite at the saturation pressure.

The resulting BET equation is as follows:

$$\frac{1}{V[\left(\frac{P_O}{P}\right)-1]} = \frac{c-1}{V_m \cdot C} \cdot \frac{P}{P_O} + \frac{1}{V_m \cdot C}$$

P = equilibrium pressure

P_O = saturation pressure

V_m = adsorbed gas volume (cm^3)

C = BET constant

(5) BET equation

The second step is to calculate the surface area. The total and specific area value can be calculated from the equations below:

$$S_{Total} = \frac{V_m \cdot N \cdot A}{V_m}$$

$$S_{Specific} = \frac{S_{Total}}{m}$$

S_{Total} = total surface area

$S_{Specific}$ = specific surface area

N = Avogadro's number (6.0221415×10^{23})

V_m = molar volume

A = adsorption cross-section area of single adsorbate molecule

m = mass of sample

(6) Surface area equation

2.7 Electrochemical Measurements

To evaluate the electrochemical performance of the developed amorphous carbon-based materials in the application of a lithium ion battery, a series of half-cell tests was performed in this work.

In the case of electrochemical evaluation of the anode materials, the half-cell consists of a Li foil and a carbon-based anode as electrodes. Figure 13 illustrates the components of the half-cell system. During charging and discharging, the intercalation and de-intercalation of lithium ions are taking place circularly.

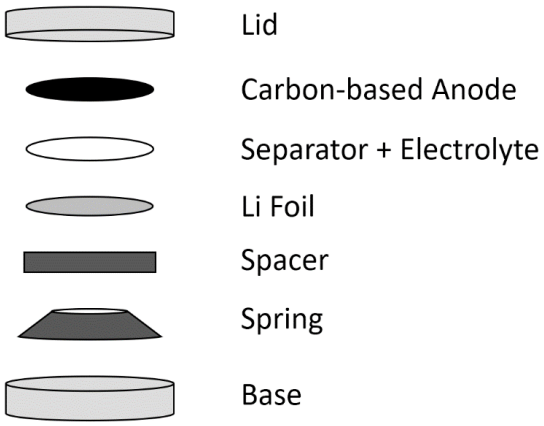

Figure 13. Illustration of a coin half-cell assembly.

In this work, the obtained carbon-based composites were employed as anodes in coin cells. The anodes were prepared by coating the slurry onto a flat Cu foil by a MTI automatic film coater or onto nickel foam with a glass rod. The slurry was composed of 80 wt.% of carbon material, 10 wt.% of Super P carbon black, and 10 wt.% of polyvinylidene fluoride binder (PVDF) in N-methyl-2-pyrrolidone (NMP) solvent. Finally, all electrodes were dried in a vacuum oven for 24 hours before coin-cell assembly.

Electrochemical tests of carbon materials were performed in CR 2032 type coin-cells with the carbon electrode as anodes and the metallic lithium foil as cathodes under room temperature, using glass-fiber as the separators. The electrolyte was composed of 1M lithium hexafluorophosphate ($LiPF_6$) in a mixture of ethylene carbonate and diethyl carbonate (1:1 vol.%). The coin cell assembly was carried out in an argon-filled glovebox with both moisture and oxygen concentrations below 0.5 ppm.

Electrochemical tests were operated in galvanostatic current charge-discharge circuits, named galvanostatic charge and discharge (GCD). GCD is used to obtain a host of

important electrochemical characteristics of the coin cells, including the discharge/charge profiles, rate capabilities and long-term cyclic performance. Rate capabilities can be obtained when various constant current densities are applied in the discharge/charge tests.

Typically, GCD is done via a battery station to provide constant current. In this work, all the electrochemical tests were carried out by a Neware BTS bench top battery test station at room temperature.

3. Design and Fabrication of Porous Carbon Nanostructures as Anodes for LIBs

3.1 Introduction

As one of the amorphous carbon materials, hard carbon anodes can deliver a higher capacity than a graphite electrode. Zheng *et al*. [26] and J.R. Dahn *et al*. [24,32] revealed the lithium-ion insertion mechanism in hard carbon, which is named "house of cards" theory. Lithium ions can adsorbed on both sides of the single graphene sheet and fill in the nanopores. Furthermore, its randomly oriented graphene sheets and large surface area provides a short path for lithium-ion diffusion, and as a result, fast charge/discharge becomes available. These characteristics make the amorphous hard carbon a potential candidate for serving as an anode material of LIBs in electric vehicles.

Of the many different precursors for hard carbon, sucrose is one of the cheapest, which has abundant agricultural sources worldwide. To meet the industrial demand, sucrose is used as a precursor in this work.

The purpose of this work is to enhance the capacity of the carbon anodes by developing interconnected high surface-area porous carbon. In this chapter, two different structural carbons are demonstrated: one is directly pyrolyzed amorphous carbon, which was carbonized at high temperature, and the other one is interconnected hollow carbon networks with a novel porous 3D structure. Both carbon materials have good rate capability and excellent cycling performance. Particularly, the carbon framework can achieve a higher reversible lithium insertion capacity than the directly pyrolyzed bulk amorphous carbon sample.

3.2 Experimental Methods

Amorphous carbon (AC)

Figure 14 schematically shows the synthesis process of the pure amorphous carbon. Sucrose (≥ 99.5% (GC), Sigma Aldrich) was used as the precursor of the amorphous carbon. 5 g of sucrose was directly heat treated in a Lindberg tube furnace in an argon atmosphere at 1100 °C (heating rate: 1 °C/min) for 6 h. Finally, the obtained bulk carbon was further ball milled into a fine powder in a MTI ball miller for 45 min. The obtained black powder was named amorphous carbon (AC).

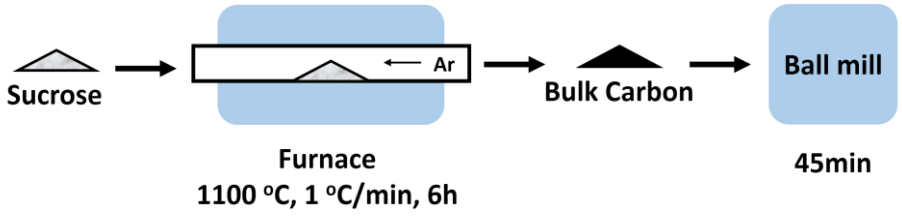

Figure 14. schematic view for synthesis of amorphous carbon (AC).

3D Interconnected Hollow Carbon Networks (CN)

To develop the unique 3D interconnected hollow carbon networks, 400 nm diameter silica spheres were used as a template.

The first step was the preparation of the SiO_2 template. 48 ml of tetraethyl orthosilicate (TEOS) precursor was dissolved in a water-ethanol solution (592 ml of ethanol, and 80 ml

of deionized water (DI)) with 25.2 ml of ammonia hydroxide (28-30%, Sigma Aldrich). After stirring (400 rpm) for 2 hours at room temperature. The obtained suspension was washed until neutral (pH=7) and dried in a MTI air convection oven at 80 ºC overnight. The bulk silica was then ground into a fine powder for further use.

Secondly, as Figure 15 illustrates, 5 g of prepared silica white powder was sonicated for two hours in 12 g of ethylene glycol (EG). The suspension was then mixed with a sucrose solution (0.5 g sucrose in 20 ml of deionized water) and sonicated for another hour to achieve a thorough dispersion. After that, the suspension was stirred rapidly at 120 ºC until dry. Then, the obtained mixture was ground and heated to 900 ºC at 5 ºC/min and held for four hours to pyrolyze the sucrose. The obtained silica-carbon composites were subsequently immersed in 10% HF (37% hydrochloric acid, Sigma Aldrich) for 24 hours to etch the silica cores. Finally, the sample was washed until neutral (pH=7) and dried in an MTI air convection oven at 80 ºC.

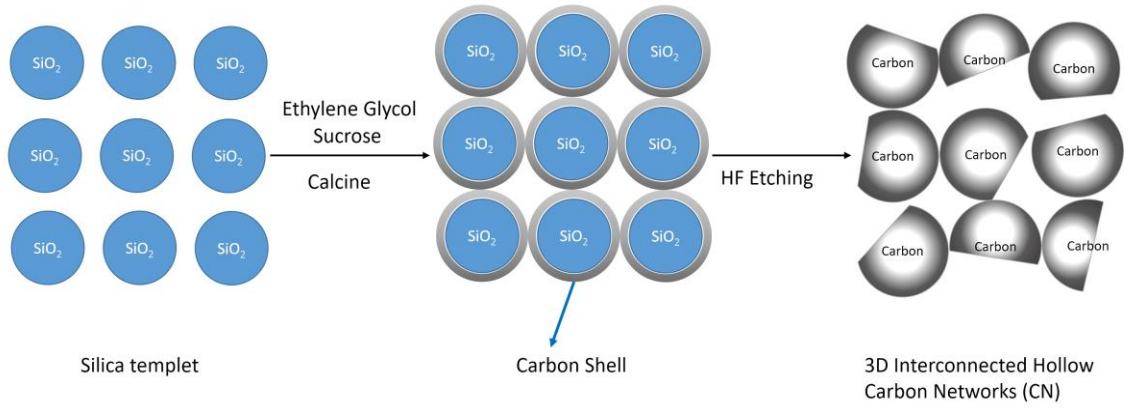

Figure 15. Schematic view for synthesis of the 3D Interconnected Hollow Carbon Networks (CN).

For the chemical and physical characterization of the synthesized amorphous carbon and 3D carbon networks, a host of analyses were utilized. Scanning electron microscopy (SEM)

and transmission electron microscopy (TEM) were employed to investigate the morphology and reveal the structure. Brunauer-Emmett-Teller (BET) and Raman spectroscopy were utilized to determine the pore-size distribution and lattice structure.

To evaluate the electrochemical performance of the prepared samples, coin cells (CR 2032) were assembled. The electrodes were prepared on Cu foils with slurries that consisted of 80 wt.% of the active material (sample), 10 wt.% Super P carbon black (conductive material), and 10 wt.% polyvinylidene fluoride (PVDF, binder). Lithium metal foils (Sigma Aldrich) were used as counter electrodes. 1 M lithium hexafluorophosphate ($LiPF_6$) with a mixture of ethylene carbonate (EC) and diethyl carbonate (DMC) (1:1 vol.%) was used as an electrolyte. Galvanostatic charge and discharge (GCD) was performed on a Neware battery testing station to investigate charge-discharge profiles and rate capabilities.

3.3 Results and Discussion

The SEM images in Figure 16 demonstrate the morphology of the obtained two carbon materials with different structures. Figure 16 (a) and (b) are SEM images of the amorphous carbon (AC). The images demonstrate that the flake-shaped carbon material has poor dispersion properties (various particle size from 10 nm to 10 μm). In contrast, Figure 16 (c) at low magnification demonstrates the 3D morphology of the interconnected hollow carbon networks (CN), indicating that the size of the carbon shell arrays are homogeneously distributed and possess a fully interconnected porous structure. Meanwhile, at high magnification, Figure 16 (d) depicts that the diameter and carbon shell thickness of CN are 400 nm and 10-15 nm, respectively. The extensive interconnection between carbon shells ensures short lithium-ion diffusion path, good electron transport, and efficient avoiding of

the nanomaterial's aggregation. Therefore, promising electrochemical properties can be expected when CN is employed as anodes for lithium ion batteries.

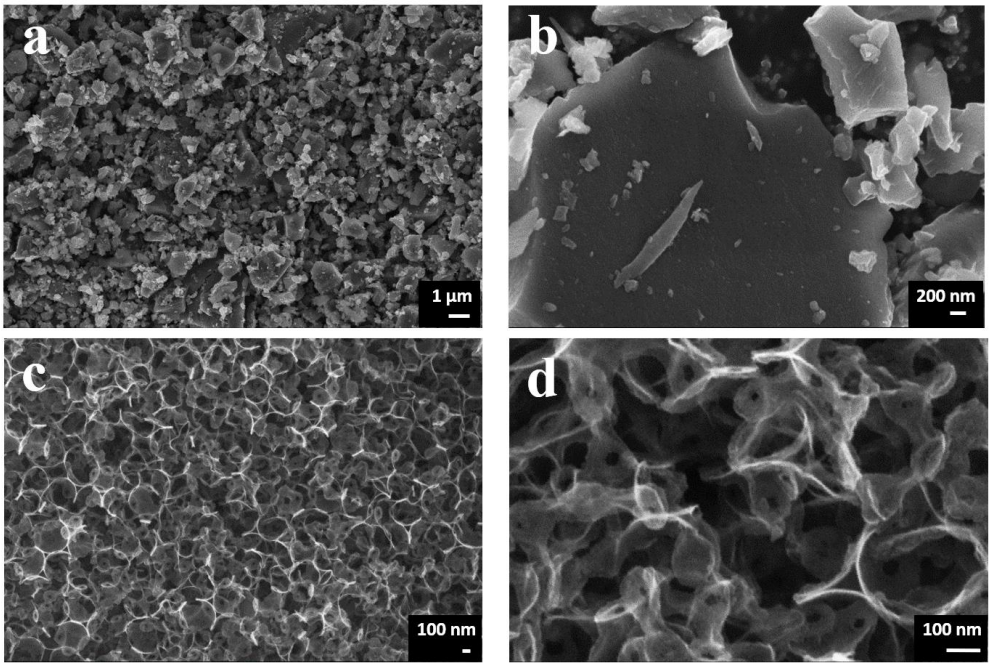

Figure 16. SEM images of (a) amorphous carbon (AC) at low magnification, and (b) high magnification, (c) interconnected hollow carbon networks (CN) at low magnification, and (d) high magnification.

To further analyze the morphology and lattice structure of the obtained AC and CN samples, transmission electron microscopy (TEM) and high resolution transmission electron microscopy (HRTEM) were used. Figure 17 (a), which has a lower magnification, gives a broad view of AC particles. Figure 17 (b) shows a close-up HRTEM image of the one-step pyrolyzed amorphous carbon at high magnification, and illustrates that the sucrose derived carbon has both non-graphitized and graphitized structures. In the non-graphitized domain, the carbon lattice possesses an amorphous (highly disordered) structure. This HRTEM image demonstrates that the obtained sucrose derived carbon possesses a partially non-

graphitized lattice structure.

The TEM images of the CN are shown in Figure 17 (c) and (d). The hollow carbon frameworks possess a finely developed spherical shape and porous structure. The interconnected carbon shells are tangential to each other, ensuring that the porous framework retains its firm structure to achieve excellent cyclic life and volume change buffering during repeated lithium ion insertion/extraction.

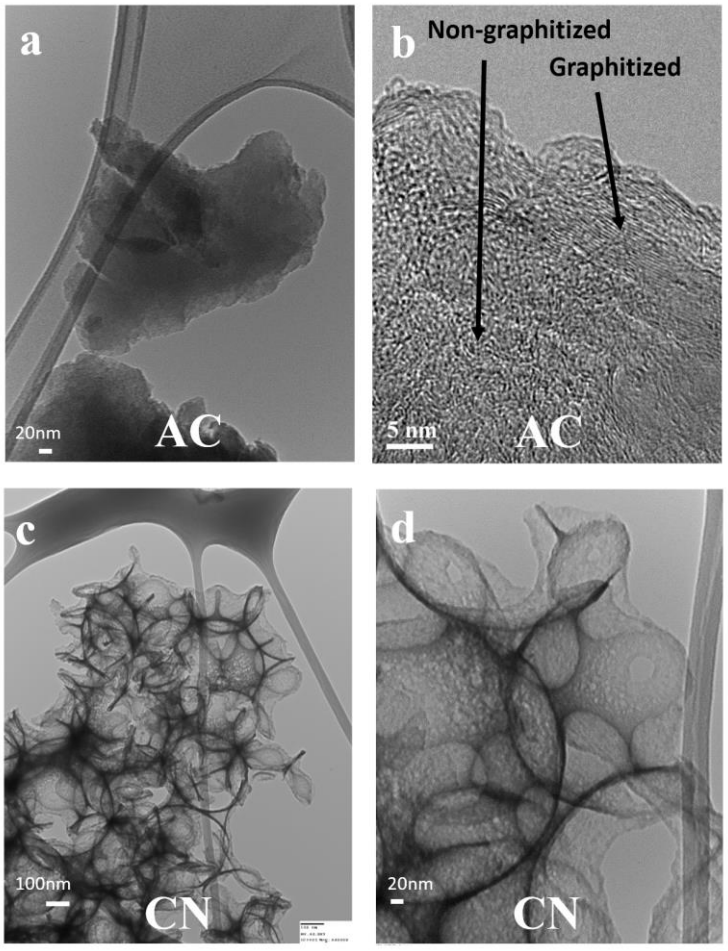

Figure 17. TEM images of AC (a), CN at low resolution (c) and high magnification (d), and HRTEM image of AC (b).

The structures of the carbon materials were further analyzed via Raman spectroscopy. The Raman spectra shown in Figure 18 demonstrates two broad bands of the defected-induced band (D-band) and the crystalline graphite band (G-band). The peaks in the range of 800-2000 cm^{-1} of the Raman shift are typical features of amorphous carbon. In AC's spectra, the Raman shift centered at 1333 cm^{-1} and 1586 cm^{-1} correspond to the D-band and G-band, respectively. While in the CN's spectra, the peaks located at 1334 cm^{-1} and 1574 cm^{-1} can be assigned to the D-band and G-band of carbon. Since the D-band relates to the disordered carbon, while the G-band corresponds to the sp^2 graphitic carbon, calculating the intensity ratio of the two bands can demonstrate the extent of the defective structure. The I_D/I_G values of AC and CN are 0.96 and 1.03, respectively, which reveals the existence of non-graphitic carbon in both samples. Therefore, AC has fewer defects than CN.

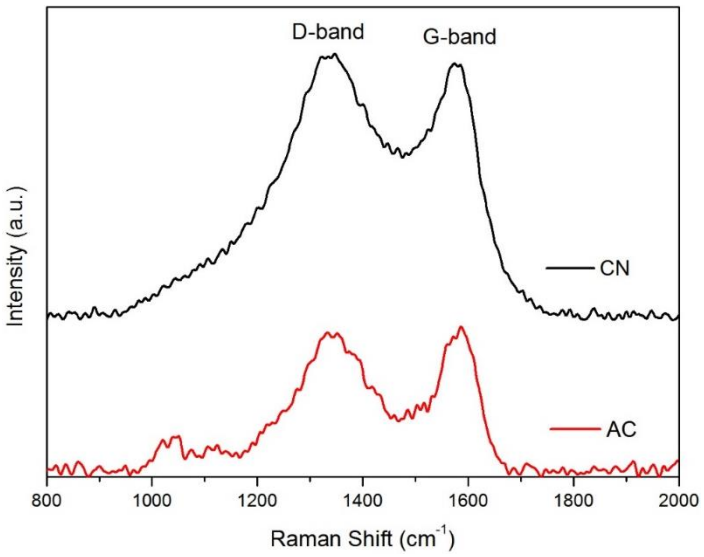

Figure 18. Raman spectra of AC and CN.

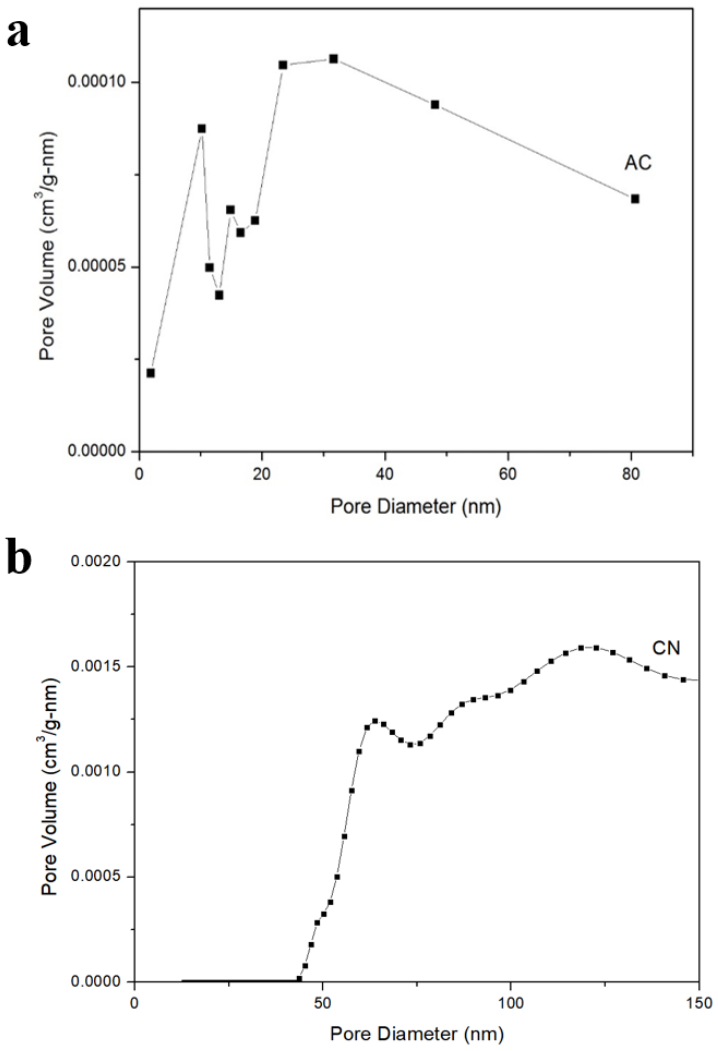

Figure 19. BET pore-size distributions of (a) AC and (b) CN, the inset shows an enlargement of the low pore diameter region of CN.

The Brunauere-Emmette-Teller (BET) surface area was measured by the analysis of N_2 adsorption-desorption isotherms. The specific surface area of AC is 61.27 m^2/g, in contrast to the 234.977 m^2/g of CN. Figure 19 (a) demonstrates the pore-size distribution calculated via BJH, indicating that the obtained AC sample has a porous structure with mesopores and macropores. The existence of mesopores in AC is believed to be a result of the decomposition gas consisting of water vapor and carbon dioxide, where both can active

carbon by burning-off at high temperatures. Meanwhile, as Figure 19 (b) shows, CN has a host of mesopores and macropores in the carbon framework (shown as the inset figure in Figure 19 b).

To analyze the application of the obtained carbon materials in lithium ion batteries, the galvanostatic charge and discharge (GCD) measurements were conducted on CR 2032 coin cells that contained obtained carbon as the anode. Figure 20 illustrates the discharge (Li^+ intercalation) and charge (Li^+ deintercalation) profiles of AC (Figure 20 a) and CN (Figure 20 b) between 0.01 and 2.00 V at a current density of 50 mA/g. In the first cycle, the electrode of AC possesses a discharge capacity of 509 mAh/g and a reversible discharge capacity of 287 mAh/g with an initial columbic efficiency of 56.4%. For the obtained CN anode, although the first discharge capacity and the reversible capacity are 1868 mAh/g and 432 mAh/g, respectively, the initial columbic efficiency is 23%, much lower than AC's. The low efficiency in the initial lithium insertion is believed to be due to the formation of a solid electrolyte interphase (SEI) layer. The high capacity of CN can be attributed to the enhanced surface area and homogenously distributed particle size. Moreover, the amorphous carbon structure provides more defects and accessible sites for lithium ion intercalation and deintercalation during the charge and discharge. The excellent electrochemical performance of CN can be attributed to the unique structure, which provides continuous pores to help electrolyte infuse efficiently and increases electron transport.

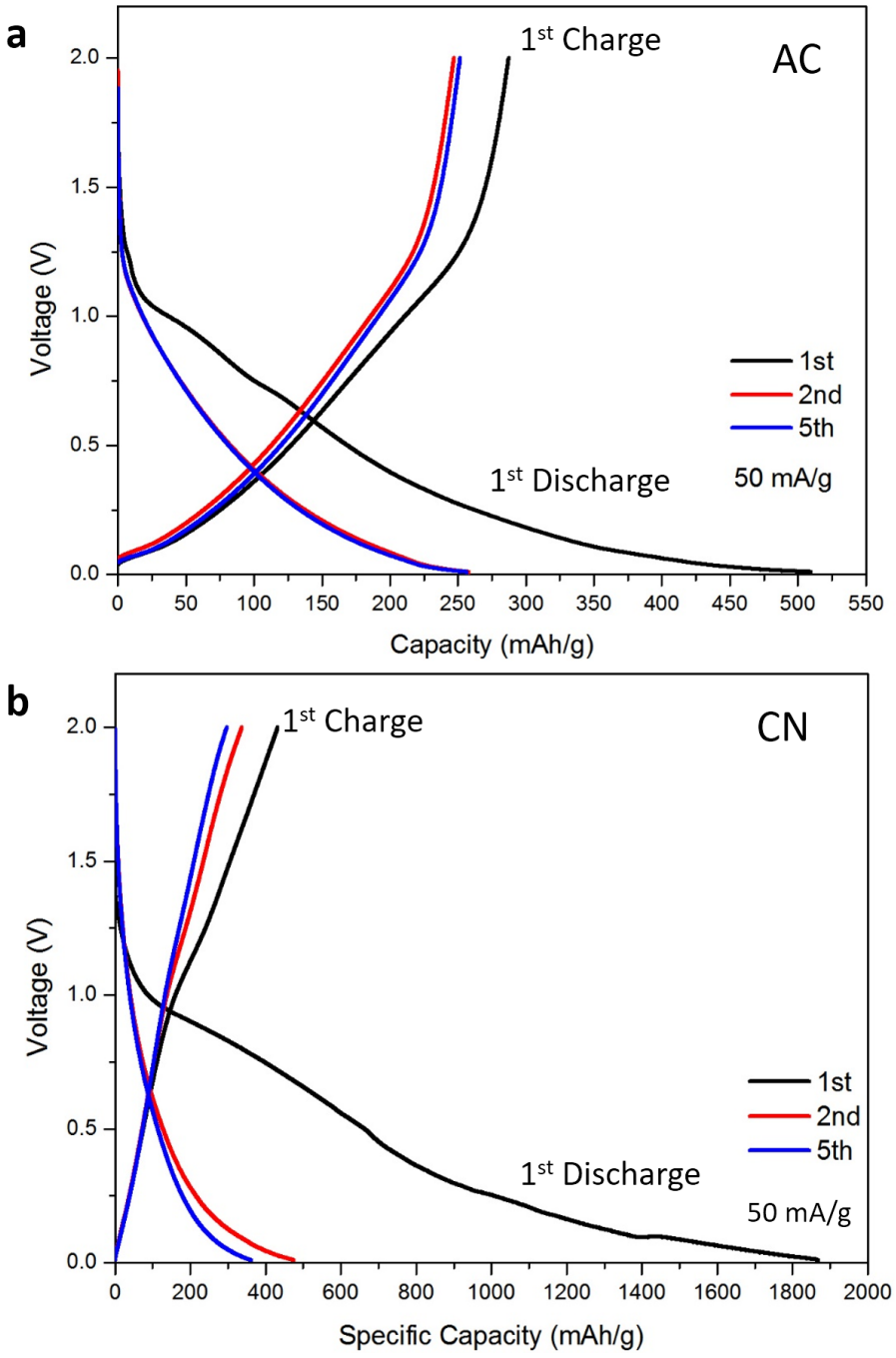

Figure 20. Charge and discharge profiles of the 1st, 2nd, 5th cycles from: (a) AC and (b) CN at a current density of 50 mA/g

In addition, the rate capability of AC and CN are demonstrated in Figure 21. It is obvious

that both samples have good rate capability. Even at a high current density (1 A/g), AC and CN still possess good reversible capacity of 138 mAh/g and 165 mAh/g, respectively. Once the current density returns back to 50 mA/g, the capacity of CN is able to resume to its previous value, which indicates CN has an excellent rate capability.

After the aforementioned rate capability test, AC and CN were further subjected to long-term cycling tests to reveal their electrochemical stability. The cycling performance of AC and CN were evaluated in a voltage range between 0.01 and 2.00 V at a current density of 1000 mA/g. As shown in Figure 22, both synthesized carbon material possess stable cycling performance. Even after 2000 cycles, AC still possesses a capacity retention of 75.78%, whereas CN even increases to 103.74%. It is obvious that both samples have excellent stability.

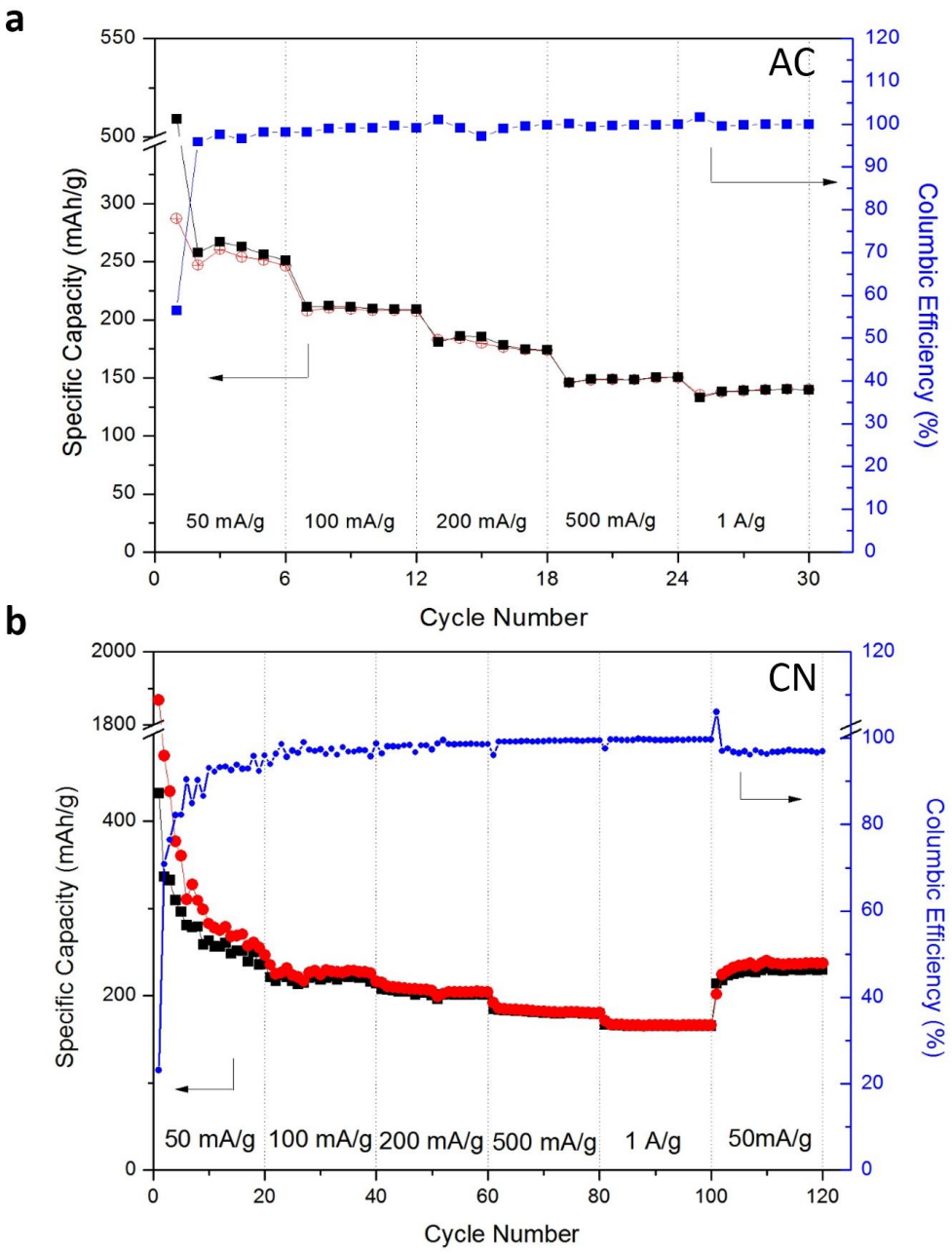

Figure 21. Rate performance of (a) AC and (b) CN

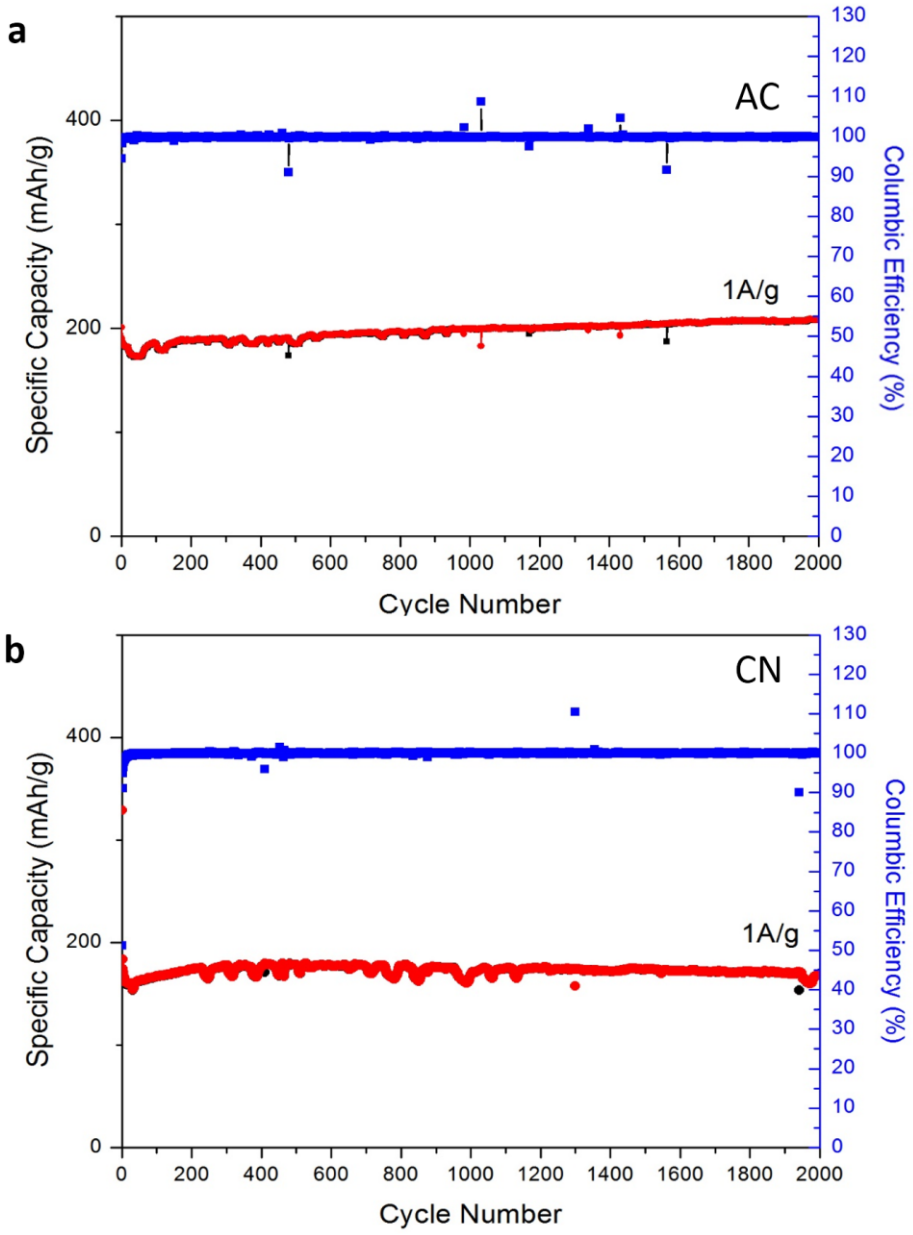

Figure 22. Charge/discharge cyclic performance of (a) AC and (b) CN at 1 A/g

3.4 Conclusions

Two different structural amorphous carbon-based materials were synthesized by direct pyrolysis and silica hard template pyrolysis of sucrose, respectively. AC was obtained by a one-step method, and resulted in good cycling performance. The sample of CN possesses a fine designed 3D interconnected structure, which is believed to be more electrically conductive and provide a large surface area for Li^+ insertion and adsorption. Compared to AC, CN has a higher reversible capacity of 432 mAh/g at 50 mA/g and a higher reversible capacity of 165 mAh/g at a high current density of 1 A/g. Both samples exhibit excellent cycling performance without obvious capacity decay after 2000 cycles.

4. Design and Fabrication of SnO_2@C 3D Nanostructures as Anodes for LIBs

4.1 Introduction

Recent years, the tin oxide is considered as one of the most promising anode materials with high reversible capacity. Theoretically, during the first charge process, SnO_2 particles irreversibly reduce to Sn metal, which provides a capacity of 711 mAh/g. During the second charge process, Li-Sn alloys are reversibly formed and provides a reversible capacity of 783 mAh/g [56]. During the charge and discharge process, the large volume expansion (300%) can lead to pulverization and loss of electrical conductivity of electrodes. As a result, the tin oxide suffers from quick capacity fade and poor rate capability [63].

To overcome the shortage of tin oxide and enhance the capacity of carbon-based anode materials, two tin oxide/carbon composites were prepared: one is core-shell tin oxide/carbon composite, where the tin oxide was coated on the dense carbon spheres; the other one is tin oxide/carbon 3D porous composite, which is developed based on the CN carbon framework. The carbon is served as a buffer for the tin oxide's volume expansion in the lithium insertion to enhance the cyclic performance and rate capability. Furthermore, carbon can compensate the loss of electrical conductivity of the composites. Both samples were activated to generate or enlarge nanopores for tin oxide embedding and further improve the lithium-ion insertion capacity. In this work, the stability of tin oxide/carbon composites has been successfully improved. Both samples achieved good rate capability and cyclic stability. Specifically, the SnO_2/CN composite can operate over 500 cycles without obvious capacity decay.

4.2 Experimental Methods

SnO_2/Carbon Spherules

Sucrose was selected as the precursor for preparing the carbon spherules. The preparation process consisted of three steps: hydrothermal carbonization, steam activation, and tin embedding. The schematic overview for this synthesis is shown in Figure 23.

First, 30.81 g of sucrose was dissolved in 60 ml of deionized water (1.5 mol/L) and 2.02 g of iron nitrate nonahydrate ($Fe(NO_3)_3 \bullet 9H_2O$) was added to the solution. The aqueous sucrose solution was placed into an autoclave and hydrothermally heated at 195 ºC for 5 hours to obtain the dewatered carbon with reduced Fe catalyst.

After being dried and ground, the black powder was calcined at 500 ºC for 2 hours in a tube furnace in argon with a heating rate of 1 ºC/min, activated in a water steam atmosphere at 900 ºC for 2 hours (5 ºC/min) to form a porous structure, and subsequently cooled naturally to room temperature. Next, the porous powder was washed with 3 mol/L hydrochloric acid (HCl) solution to remove the catalyst and further washed with deionized water until a pH of 7 was reached.

Finally, 0.0213 g of $SnCl_2 \bullet 2H_2O$ (tin chloride dihydrate (II) 98%, Sigma Aldrich) was dissolved in 6 ml of ethanol. The $SnCl_2$ solution and prepared activated carbon spherules (ACS) were then mixed and sonicated to achieve a thorough dispersion. This solution was stirred until dry. The black powder was subsequently pyrolyzed in a tube furnace at 600 ºC for 3 hours (5 ºC/min) in argon atmosphere. The obtained sample was named tin oxide/carbon spherules (SnO_2/CS).

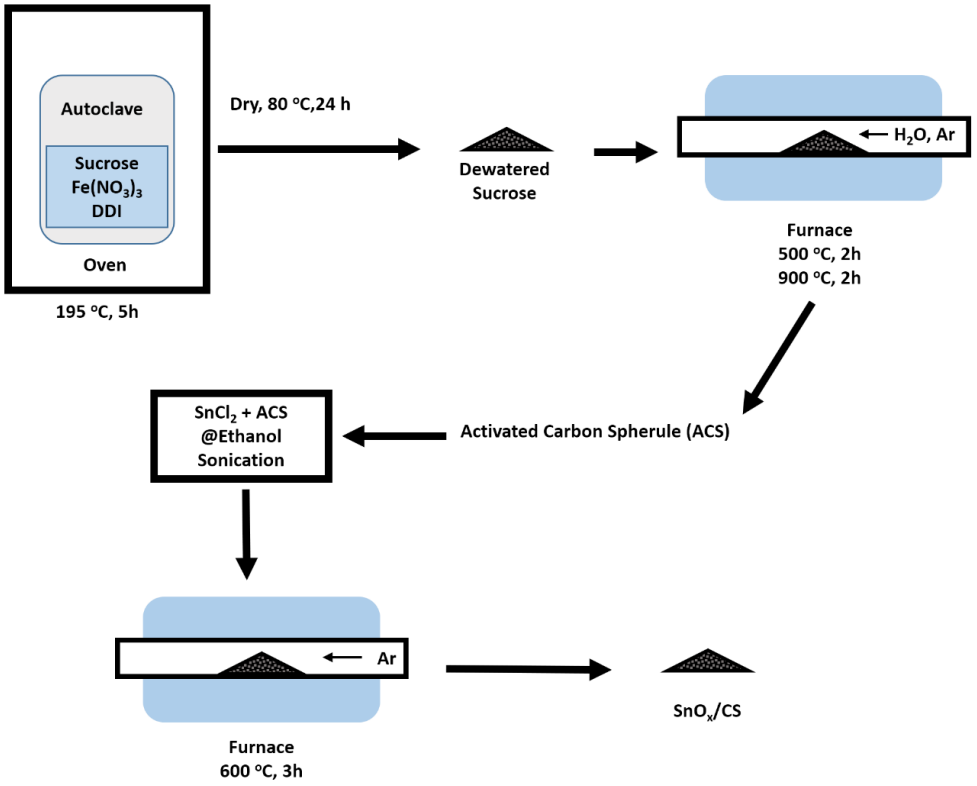

Figure 23. Schematic overview for synthesis of tin oxide/carbon spherules (SnO_2/CS).

SnO_2/Carbon Networks (SnO_2/CN)

The carbon networks were prepared via a method similar to that of which was in chapter 4. The silica template was prepared with a homogenous diameter of 400 nm. 1 g of sucrose was dissolved in 20 ml of deionized water as a precursor solution. Then the precursor solution was mixed and sonicated with a silica @ ethylene glycol (EG) (mass ratio, 5:12) suspension. After being stirred at 120 °C to dry, the white mixture was ground and heat treated in a tube furnace at 900 °C for four hours at 5 °C/min in argon. The silica template was etched by 4 mol/L NaOH and stirred at 350 rpm for five days in a 85 °C water bath. Next, the black particles were centrifuged and washed with deionized water.

To enhance the pore-size and surface area, KOH (potassium hydroxide, Sigma Aldrich) was used for activation. The obtained carbon shells were thoroughly mixed with KOH (KOH/carbon mass ratio was 3:1) in 50 ml DI water. After being dried in oven, the sample was heated at 800 ºC for one hour in a tube furnace and cooled naturally. The sample was immersed in 5% HCl solution to remove by-products and then washed with deionized water.

Finally, the tin oxide was embedded into the porous carbon shells with a similar method mentioned in the preparation of SnO_2/CS. 0.0200 g of carbon was mixed with 0.0043 g of $SnCl_2 \cdot 2H_2O$ in ethanol and sonicated before being dried at 80 ºC under stirring. After that, the mixture was heated up to 600 ºC for 3 hours. The obtained sample was named tin oxide/ carbon networks (SnO_2/CN). The sequence of preparation is presented in Figure 24.

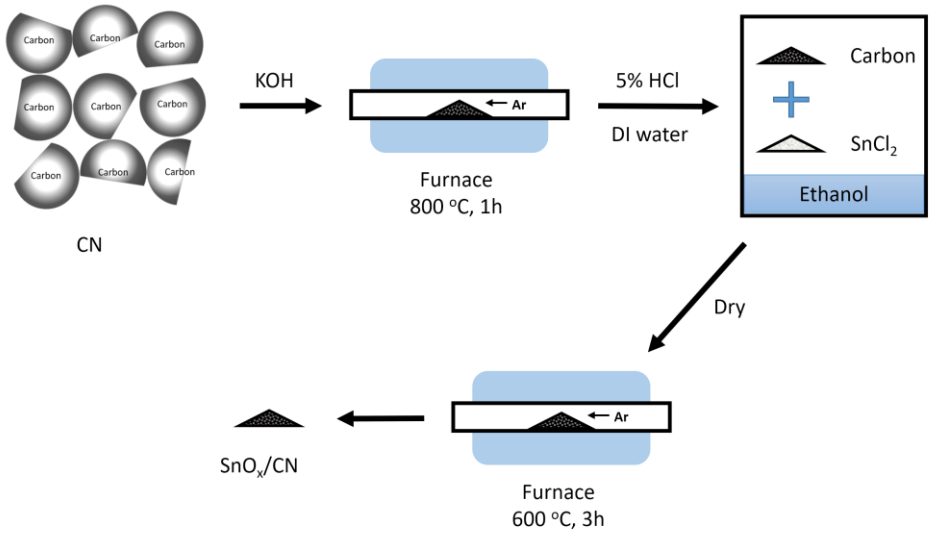

Figure 24. Schematic view for the synthesis of tin oxide/carbon networks (SnO_2/CN).

For chemical and physical characterization of the obtained tin oxide/carbon composites, a series of physical and electrochemical analyses were used to reveal the material's structure on a nanoscale and evaluate the electrical performance as anodes for lithium ion batteries.

The images of scanning electron microscopy (SEM) and transmission electron microscopy (TEM) mapped the surface morphology and structure. Utilizing the X-ray diffraction (XRD) technique, the existence of tin oxide was identified from the scattering patterns. The quantity of tin oxide was further analyzed by thermogravimetric analysis (TGA). Moreover, the Raman spectroscopy and Brunauer-Emmett-Teller (BET) analytical techniques provided the information about pore-size distribution and carbon structure.

Coin cells (CR 2032) were assembled for electrical analysis. The electrodes were prepared by coating slurries on nickel foam. The slurries were mixtures of 80 wt.% of the active material (sample), 10 wt.% Super P carbon black (conductive material), and 10 wt.% polyvinylidene fluoride (PVDF, binder). Lithium metal foils (Sigma Aldrich) were used as counter electrodes. 1 M lithium hexafluorophosphate ($LiPF_6$) with a mixture of ethylene carbonate (EC) and diethyl carbonate (DMC) (1:1 vol.%) was used as electrolyte. A Neware BTS battery testing station was used for galvanostatic charge and discharge (GCD) testing to investigate charge-discharge profiles and rate capabilities.

4.3 Results and Discussion

Scanning electron microscopy (SEM) was utilized for morphology analysis. As shown in Figure 25 (a) and (b), the SnO_2/CS composite possesses a carbon core and SnO_2 coated shell. The diameter of the composite is in a range of 4 μm – 12 μm, while the majority of the particles are approximately 10 μm in diameter. Figure 25 (c) and (d) demonstrate the morphology of the KOH activated carbon networks (ACN). As the concentration of the precursor solution increases, the thickness of the carbon shells consequently increased as well. Compared with the previous CN described in the Chapter 4, the activated shells have

more pores. The porosity of the carbon frame could contribute to tin oxide particle intake. For the SnO_2/CN composite, shown in Figure 25 (e) and (f), tin oxide particles are clearly visible on the carbon framework. Compared with the morphology of activated carbon networks, a friction of the SnO_2/CN collapsed owing to the long time stirring during the final procedure.

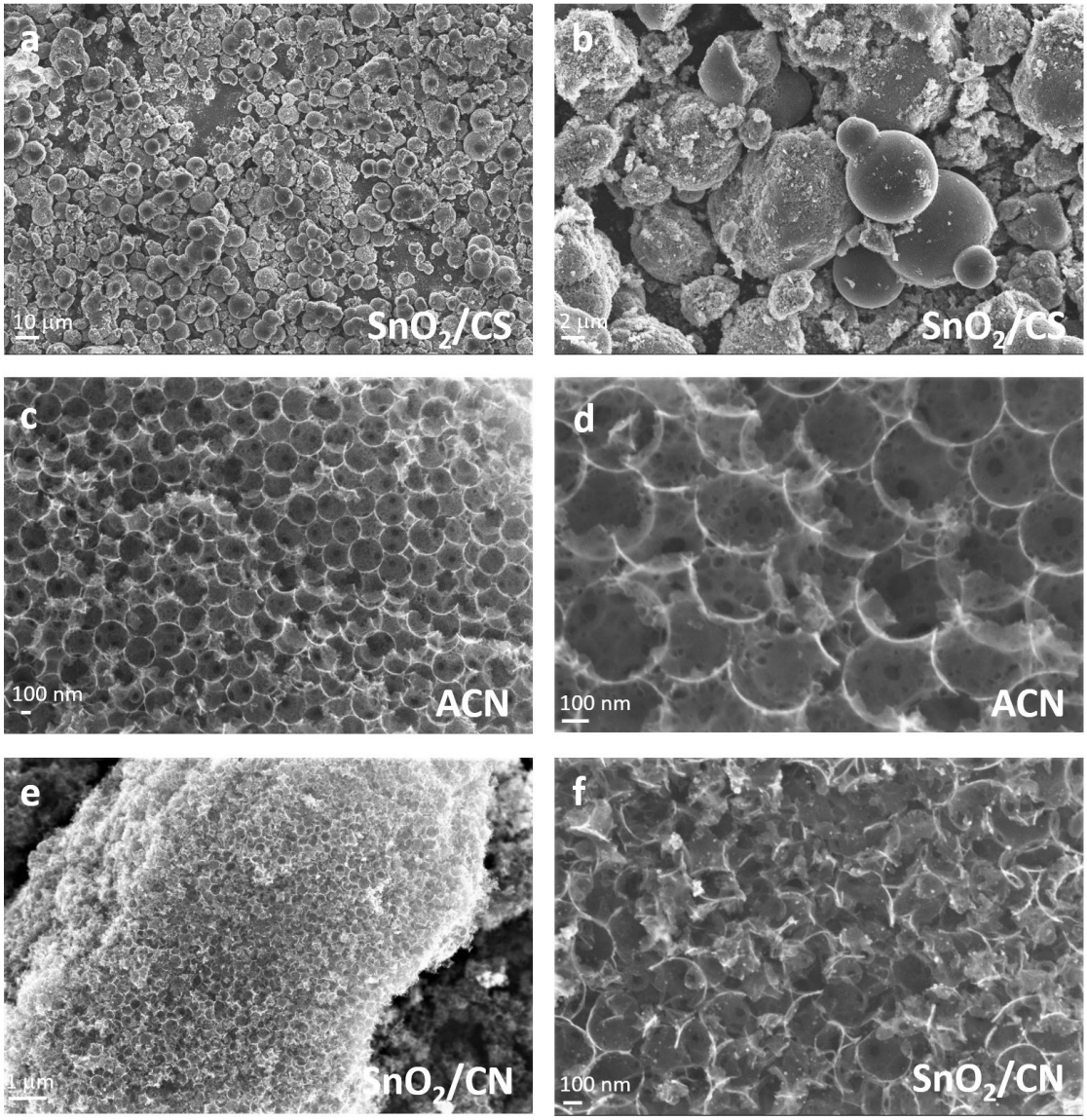

Figure 25. SEM images of SnO_2/CS (a) and (b), activated CN (c) and (d), SnO_2/CN (e) and (f).

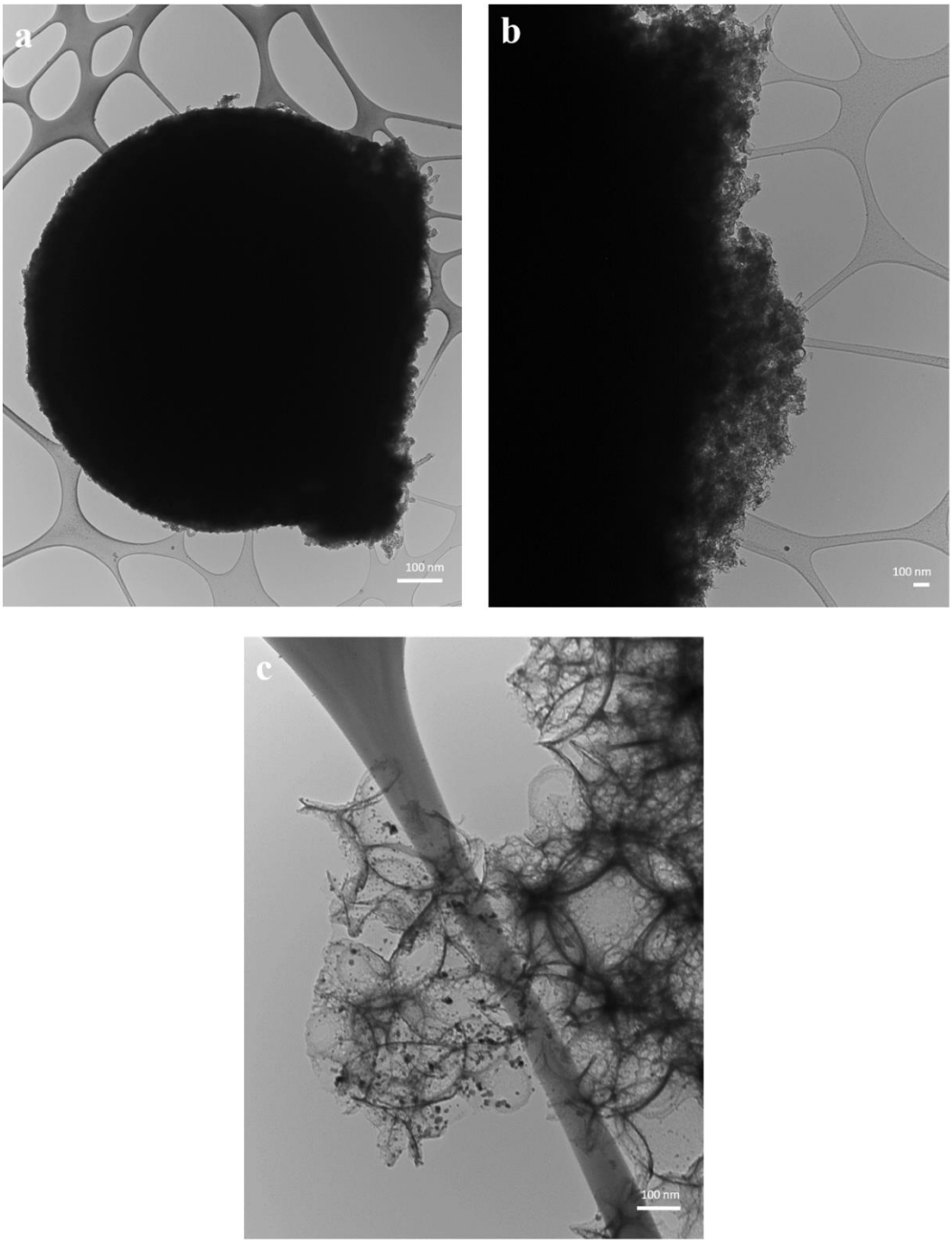

Figure 26. TEM images of SnO_2/CS (a) and (b), SnO_2/CN (c).

The morphology of SnO_2/CS was further analyzed by transmission electron microscopy (TEM). As shown in Figure 26 (a) and (b), SnO_2 nanoparticles were coated on the surface

of carbon microspherules. The image of Figure 26 (c) clearly demonstrates that the structure of SnO_2/CN components are spherical carbon shells with uniformly dispersed tin oxide nanoparticles.

The two structurally different SnO_2/C composites' crystallography is analyzed via X-ray diffraction (XRD) technique. The identified peaks in the XRD patterns of SnO_2/CS and SnO_2/CN, demonstrated in the Figure 27, are perfectly in accordance with that of tetragonal tin oxide. Meanwhile, no peaks corresponding to metallic tin are found in both patterns, indicating that tin atoms only exist as SnO_2 in both composites.

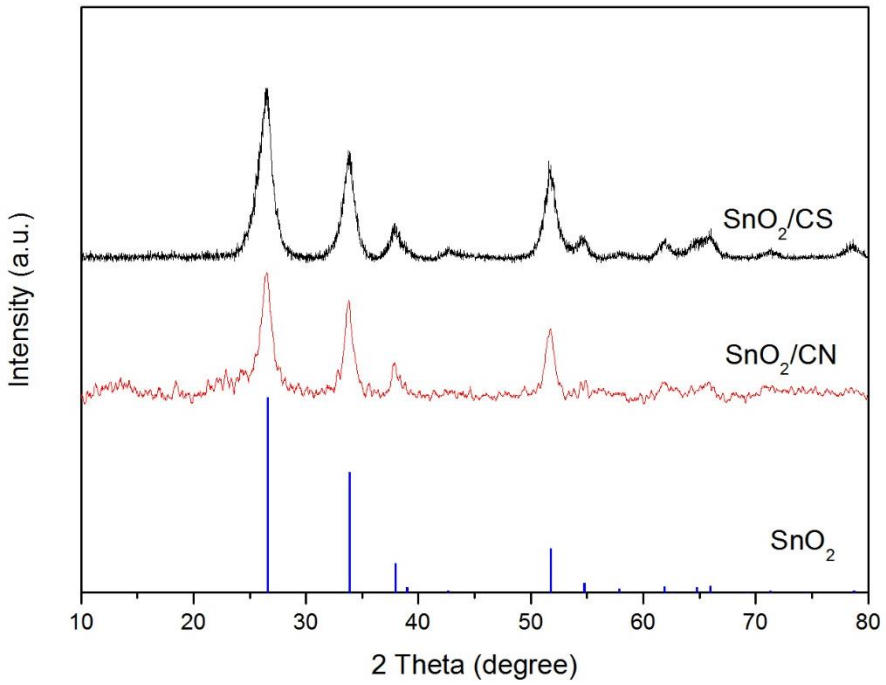

Figure 27. X-ray diffraction (XRD) patterns of SnO_2/CS and SnO_2/CN.

Raman spectroscopy was used to characterize the carbon structure in both composites. The Raman spectra of the two composites, shown in Figure 28, depict D-band (defected and amorphous carbon) and G-band (graphitic carbon) broad peaks in a Raman shift range of 800-2000 cm^{-1}. In the spectra of SnO_2/CS, the D-band is centered at 1338 cm^{-1} and the G-

band is centered at 1570.5 cm^{-1}, while the SnO_2/CN's spectra possesses the D-band at 1338 cm^{-1} and the G-band at 1586 cm^{-1}. The I_D/I_G ratios were 1.4376 and 1.09807 for SnO_2/CS and SnO_2/CN, respectively. The higher I_D/I_G value of SnO_2/CS, implies it has more defects in its carbon structure than SnO_2/CN does.

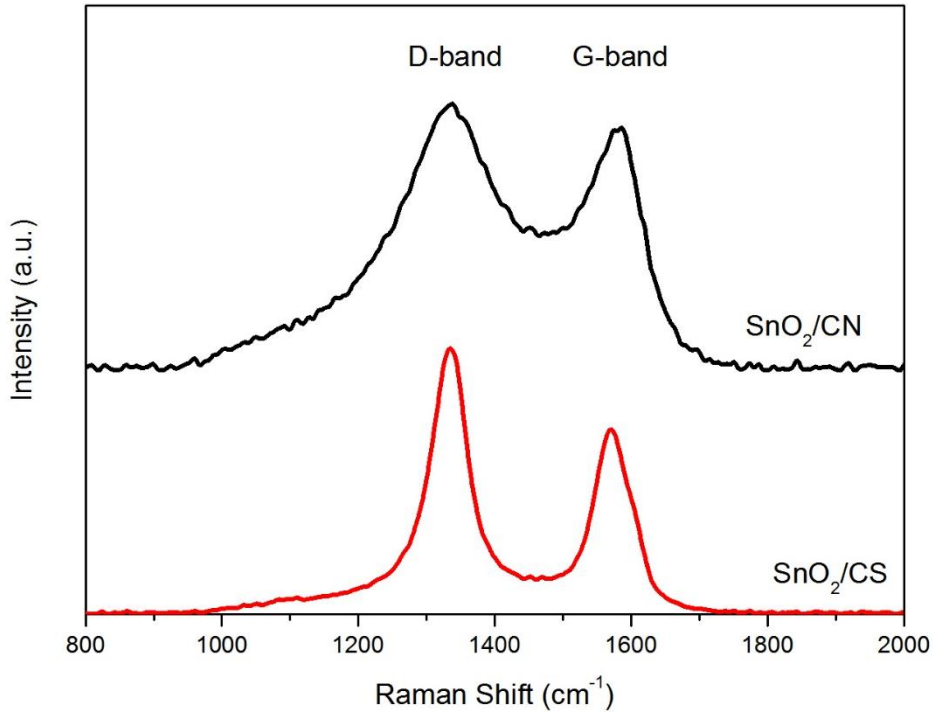

Figure 28. Raman spectra of SnO_2/CS and SnO_2/CN composites.

The nitrogen adsorption-desorption was measured to obtained information on surface area and pore-size distributions of SnO_2/CS and SnO_2/CN. As a result of the vapor activation and KOH activation applied on carbon spherules and carbon networks, the surface areas of both samples were significantly enlarged. The Brunauer-Emmett-Teller (BET) surface area of SnO_2/CS is 225.7 m^2/g, and that of SnO_2/CN is 823.3 m^2/g. Moreover, the carbon activation creates more mesopores (2-50 nm) in both samples (shown in Figure 29). Since lithium ions not only intercalate between graphene layers but also absorbed on the internal surface of nanopores in amorphous carbon, the existence of the mesopores can provide

extra capacity for the porous carbon.

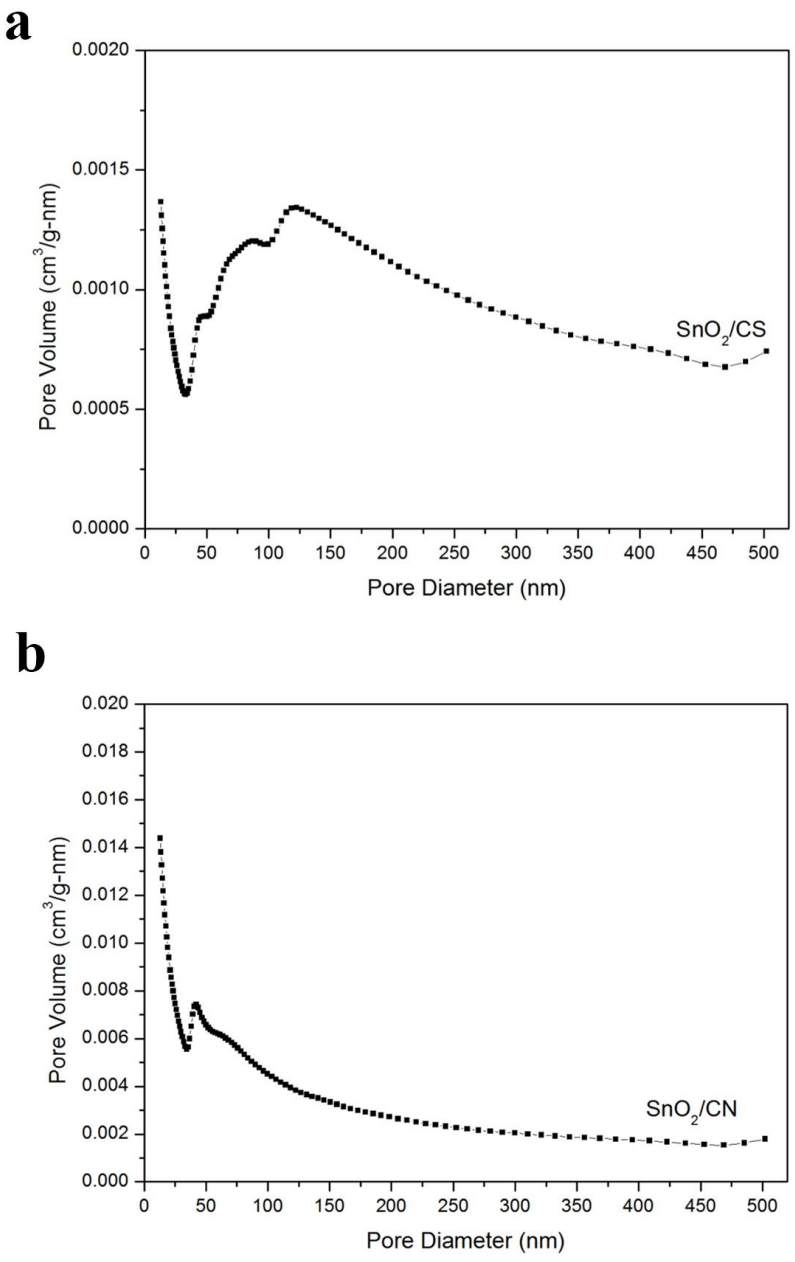

Figure 29. BET pore-size distribution of (a) SnO_2/CS and (b) SnO_2/CN.

To determine the SnO_2 content in the composites, TGA measurements was applied on SnO_2/CS and SnO_2/CN. The TGA curves are shown in Figure 30. The two samples were

heated up to 800 ºC (10 ºC/min) in air atmosphere. In both curves, strong weight losses exist in a temperature range of 300-600 ºC are related to carbon oxidation. The final weight indicating that SnO_2/CS contains 40.6 wt.% tin oxide and SnO_2/CN contains 16.1 wt.% tin oxide, respectively.

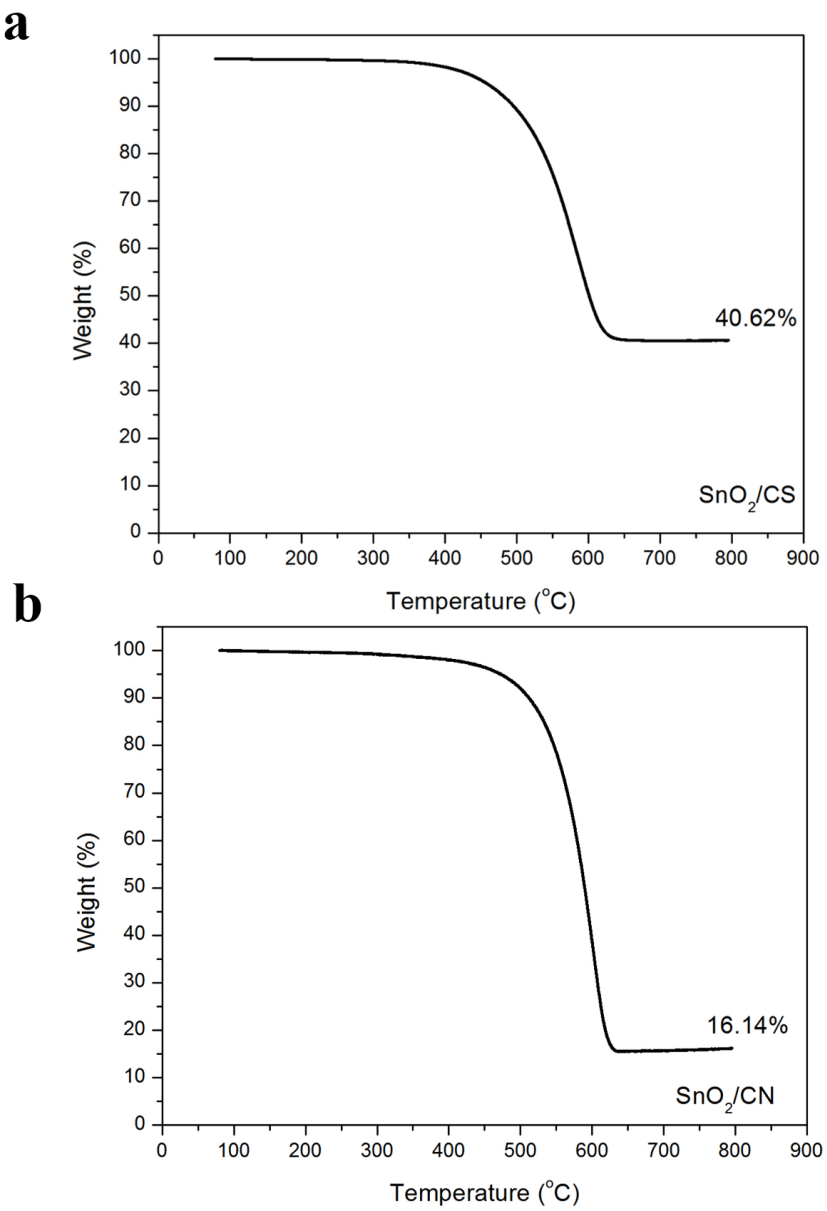

Figure 30. TGA curves of (a) SnO_2/CS and (b) SnO_2/CN.

To characterize the electrochemical performance of the obtained SnO_2/C composites as anodes of lithium ion batteries, the galvanostatic charge and discharge (GCD) measurements were conducted on CR 2032 coin cells.

1) SnO_2/CS

Electrochemical properties of the as-prepared SnO_2/CS were evaluated by galvanostatic charge and discharge measurements, as shown in Figure 31. Figure 31 (a) shows the typical charge/discharge profiles at a cutoff voltage of 0.01-2.00 V and a current density of 50 mA/g. In the first cycle, the initial discharge capacity of SnO_2/CS is 1712.17 mAh/g, and the reversible capacity is 650.33 mAh/g. Considering that 40.6 wt.% of tin oxide is coated on the carbon spheres and 59.38 wt.% of the composites is carbon, the theoretical capacity can be calculated to be 827.73 mAh/g, based on 1494 mAh/g of SnO_2 and 372 mAh/g of carbon. The initial lithium insertion capacity of SnO_2/CS composite is much higher than the theoretical capacity, which is believed to be due to two aspects: first reason is the large surface area on which lithium ions can adsorb, and second reason is the disordered and porous carbon structure that provides abundant active sites in defective carbon planes in which lithium can fill.

The initial columbic efficiency of SnO_2/CS is as low as 38.0%. In the subsequent second and third cycle, the columbic efficiency is increased, indicating a high charge and discharge reversibility. Furthermore, the high irreversible capacity in the first cycle is associated with the formation of SEI on the SnO_2/CS surface and the formation of Li_2O during the first step lithiation. The charge-discharge reaction mechanism of tin oxide is as follows:

$$SnO_2 + 4\,Li^+ + 4\,e^- \rightarrow Sn + 2\,Li_2O \quad (5)$$

$$Sn + x\,Li^+ + x\,e^- \rightarrow Li_xSn (0 \leq x \leq 4.4) \quad (6)$$

In the first reaction step, which is irreversible at low voltage (0-1.5 V) [53], the in situ formation of Li_2O leads to 711 mAh/g of capacity. After that, Sn can alloy with lithium ion in the second step, which provides 783 mAh/g of reversible capacity. However, the Sn can easily to form an SEI film, which results in the irreversible capacity in the following cycles.

To further examine the rate capability of the resulting SnO_2/CS, the charge and discharge test was carried out at different current densities. The capacity of the SnO_2/CS composites are 745.6, 518.0, 461.9, 378.1, 259.0, and 146.6 mAh/g at current densities of 50, 100, 200, 500, 1000, and 2000 mA/g, respectively The stepped cyclic rate performance at different current densities is shown in Figure 31 (b). The SnO_2/CS composite exhibits a good rate performance while increasing the current density. However, in the first ten cycles at 50 mAh/g, due to Sn easily reacting with electrolyte, the capacity shows a downward trend. After that, the electrode become stable.

Besides rate capability, the cycling stability of anode materials is also very important for LIBs. A cyclic performance test was conducted after a 120-cycle rate capacity test. The long-term cycling performance at 1000 mA/g with a cut-off voltage of 0.01-2.00 V can be seen in Figure 31 (c). Due to the carbon spherule core of the composite, which is acts as a buffer for the large volume change during the lithium insertion and desertion, the collapse of the tin oxide shell can be prevented and a longer lifespan can be achieved. After 300 cycles at a current density of 1000 mA/g, SnO_2/CS anode can retain a capacity of 158.8 mAh/g with a capacity retention of 70.88%, clearly showing excellent cycling stability.

a

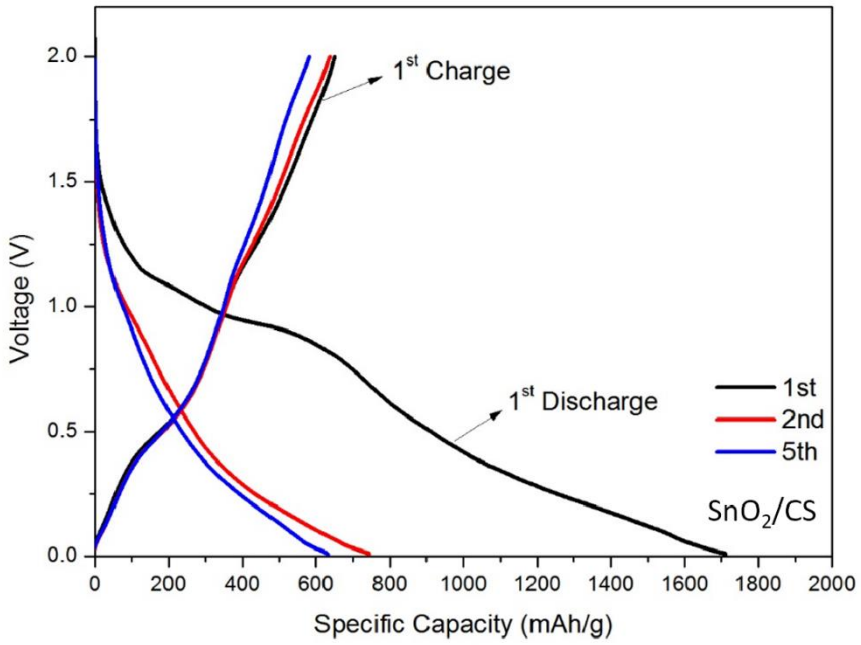
1st Charge
1st Discharge
1st
2nd
5th
SnO2/CS
Voltage (V)
Specific Capacity (mAh/g)

b

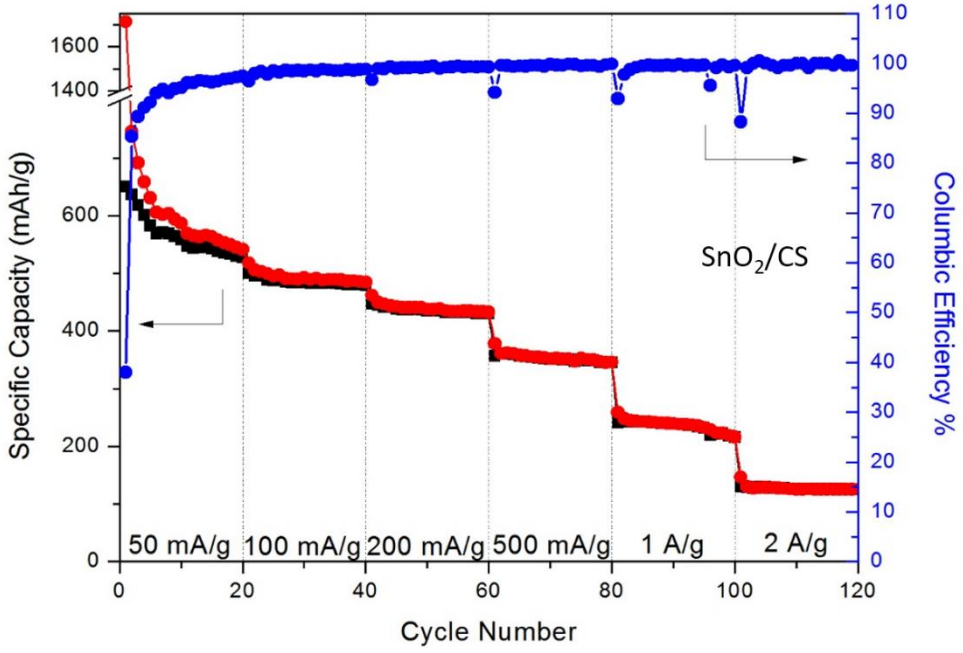
SnO2/CS
50 mA/g
100 mA/g
200 mA/g
500 mA/g
1 A/g
2 A/g
Specific Capacity (mAh/g)
Columbic Efficiency %
Cycle Number

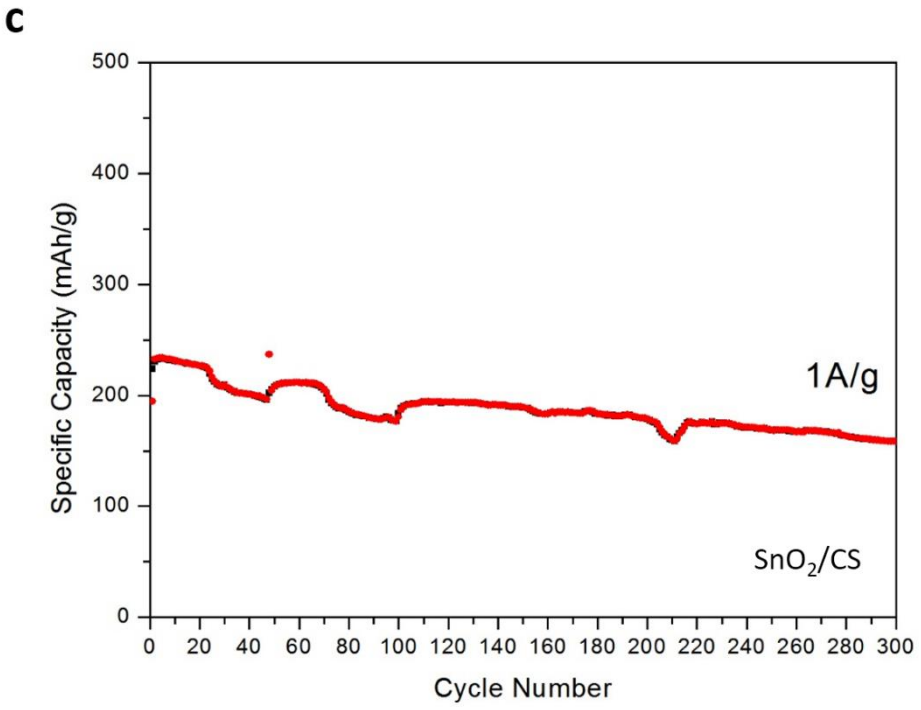

Figure 31. (a) Charge and discharge profiles of the 1st, 2nd, 5th cycles at 50 mA/g, (b) rate performance, and (c) cycling performance of SnO_2/CS at 1 A/g.

2) SnO_2/CN

The electrochemical performance of SnO_2/CN was evaluated by galvanostatic charge and discharge (GCD) method. The charge and discharge profiles for the first, second, and fifth cycle of SnO_2/CN are depicted in Figure 32 (a). The SnO_2/CN anode delivers a high capacity of 2412.4 mAh/g in the first discharge and 594.98 mAh/g in the first charge. Considering that 16.14 wt.% of tin oxide is coated on the carbon sphere, and 83.86 wt.% of the composite is carbon, the theoretic capacity can be calculated to be 438.36 mAh/g, based on 783 mAh/g reversible capacity of SnO_2 and 372 mAh/g of carbon. The reversible capacity of the SnO_2/CN composite is higher than the calculated theoretical capacity, which

is owing to the large surface area and the abundance of defects in the amorphous carbon structure. The initial columbic efficiency of this composite can be calculated to be 24.7%. The high initial irreversible capacity of this sample is associated with the irreversible formation of Sn and Li_2O (Reaction (1)) in the first cycle and the SEI film formation on the anode surface. An obvious voltage plateau at 0.9 V can be seen in the first discharge curve, which is associated with the structural deterioration and electrolyte decomposition.

To further analyse the electrochemical performance of the obtained SnO_2/CN composite, the rate capability was investigated at different current densities. As shown in Figure 32 (b), the capacity has a downward trend while the current density is increasing. The capacity of the SnO_2/CN composites are 673.1, 392.0, 319.2, 282.1, and 234.0 mAh/g at current densities of 50, 100, 200, 500, and 1000 mA/g, respectively. To investigate the stability of the composite, the anode was subjected to a continuous long-term cyclic test after the 50-cycle rate capability test. Figure 32 (c) shows the cycling stability of the SnO_2/CN composite at a constant current of 1000 mA/g with a cut-off voltage between 0.01 and 2.00 V. The unique structural composite shows an excellent stability. The electrode can still deliver a capacity of 210.74 mAh/g with a capacity retention of 95.5% even after 500 cycles. Compared to the SnO_2/CS composite spherules, the porous framework exhibits an improved stability. Presumably, the carbon shells can act as a buffer to counteract the large volume expansion (V = 260%, Sn → $Li_{4.4}Sn$) during the lithiation and enhance the electrical conductivity as well. Embedding SnO_2 in the pores can prevent the capacity fade that is caused by tin oxide pulverization.

a

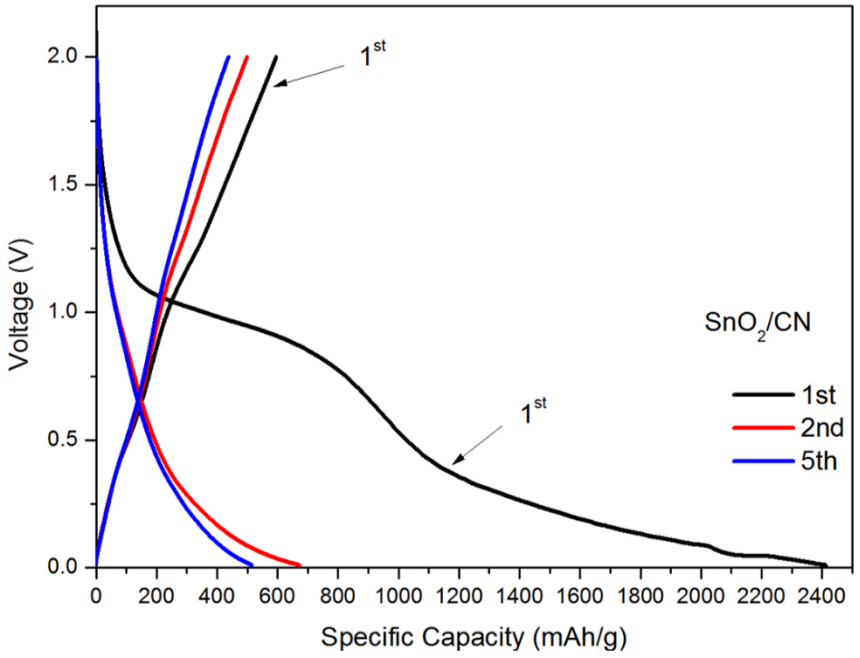
Voltage (V)
Specific Capacity (mAh/g)
1st
1st
SnO2/CN
1st
2nd
5th

b

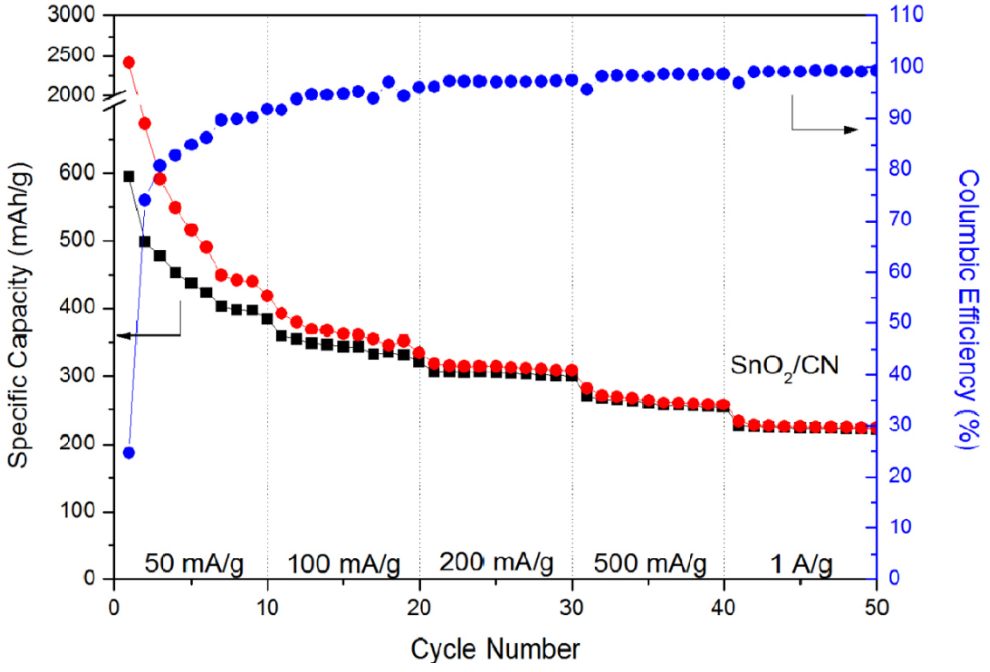
Specific Capacity (mAh/g)
Columbic Efficiency (%)
Cycle Number
SnO2/CN
50 mA/g
100 mA/g
200 mA/g
500 mA/g
1 A/g

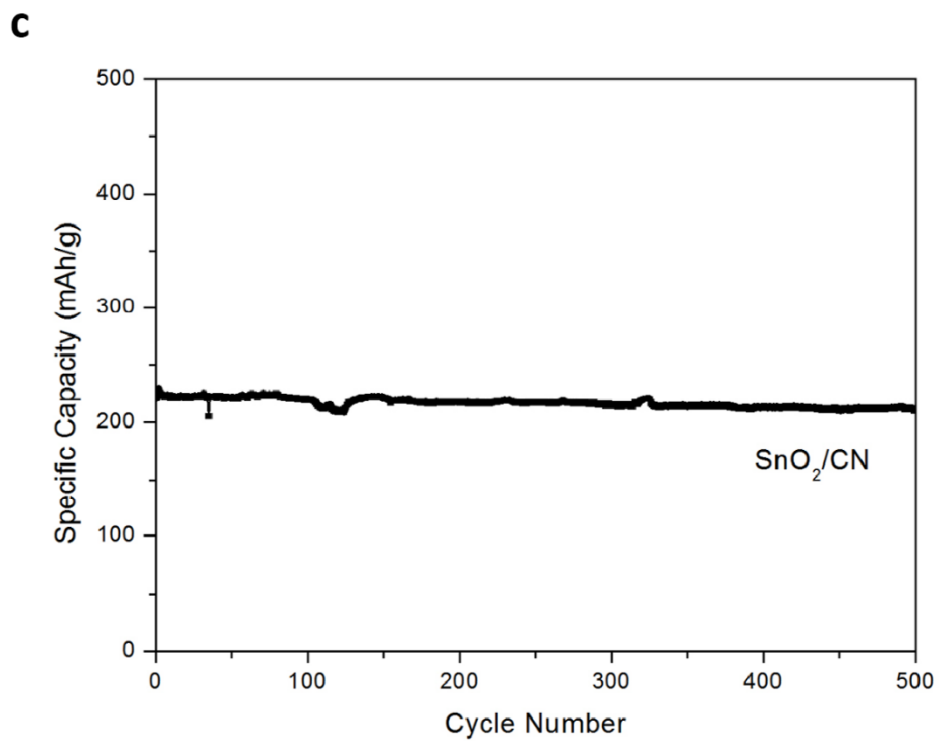

Figure 32. (a) Charge and discharge profiles of the 1st, 2nd, and 5th cycles at 50 mA/g, (b) rate performance, and (c) cycling performance for SnO_2/CN at 1A/g.

4.4 Conclusions

Porous tin oxide/carbon composites were synthesised with two different structures. The carbon activation process was applied in the preparations of both samples and had two purposes. First, it served to enlarge the surface area and produce nanopores for lithium ion insertion or adsorption between the graphene sheets and into the nanopores. Second, it provided macropores on the surface for tin oxide embedding.

In the dense core-shell SnO_2/CS composite (40.6 wt.% tin oxide), the carbon core served as a buffer to overcome the severe volume expansion problem. The SnO_2/CN anode delivered a high reversible capacity of 594.98 mAh/g in the first cycle at a current density of 50 mAh/g. Furthermore, its cycling performance is notable. SnO_2/CS can have a capacity of 158.786 mAh/g with a capacity retention of 70.88% at 1 A/g after 300 cycles.

In the novel 3D porous SnO_2/CN composite (16.14 wt.% tin oxide), a small amount of tin oxide nano particles were well distributed on the surface of an organized carbon framework. As the 3D carbon networks are interconnected and the porous carbon itself can buffer the tin oxide volume expansion, the composite's structure is believed to be extremely stable during charge/discharge. Moreover, the interconnected carbon network provides a continuous path for electron transit and compensates for the loss of electrical conductivity of the tin oxide/carbon composites. As a result, the SnO_2/CN has better stability than the SnO_2/CS. It can deliver a capacity of 210.74 mAh/g at 1000 mA/g with a capacity retention of 95.5% even after 500 cycles, which is remarkable for tin oxide/carbon composite anode materials.

5. Conclusions of Thesis and Future Works

Lithium ion batteries have a promising future as the next generation of energy storage devices for portable device and electric vehicle (EV) applications. To meet the increasing demands for the large-scale batteries, two amorphous carbon materials and two tin oxide/carbon composites have been investigated in this thesis. The major features of this thesis are as follows:

(a) Among the two amorphous carbon anode materials, the carbon networks (CN) present a better lithium insertion capacity. The increase in performance can be attributed to an extensive available specific surface area and uniformly distributed particle size. The interconnection between each carbon shell provides a shorter lithium-ion diffusion path and improves the material stability. Both AC and CN possess excellent cycling performance. Nevertheless, the initial columbic efficiency of CN is very low, so further work is needed to resolve this shortcoming.

(b) The tin oxide/carbon spheres have a core-shell structure. The porous carbon core successfully enhanced the structural stability by buffering the tin oxide shells' volume expansion during lithium insertion.

(c) The tin oxide/carbon networks were obtained by embedding tin oxide nanoparticles in the porous surface of the carbon framework. The carbon framework provides a firm structure for the tin oxide to circumvent the electrode degradation and compensate for the loss of electrical conductivity of the composites. Additionally, the SnO_2/CN has an excellent cycling performance and high lithium insertion capacity. However, the columbic efficiency needs to be improved in future work.

Although the electrochemical performance of these obtained anode materials is good, more research needs to be done to improve the columbic efficiency and the volumetric energy

density. One approach would be to increase the thickness of the carbon networks and reduce the diameter of the silica template to diminish the specific surface area and the formation of a SEI film. Another approach would be to develop a dense SnO_2/carbon/SnO_2 sandwich spherical material to improve the volumetric energy density.

Reference

(1) Nagaura, T.; Tozawa, K. Lithium Ion Rechargeable Battery. *Prog. Batter. Sol. Cells* **1990**, *9*, 209.

(2) Tarascon, J.-M.; Armand, M. Issues and Challenges Facing Rechargeable Lithium Batteries. *Nature* **2001**, *414* (6861), 359–367.

(3) Loeffler, N.; Bresser, D.; Passerini, S. Secondary Lithium-Ion Battery Anodes: From First Commercial Batteries to Recent Research Activities. *Johnson Matthey Technol. Rev.* **2015**, *59* (1), 34–44.

(4) Ji, L.; Lin, Z.; Alcoutlabi, M.; Zhang, X. Recent Developments in Nanostructured Anode Materials for Rechargeable Lithium-Ion Batteries. *Energy Environ. Sci.* **2011**, *4* (8), 2682.

(5) Goriparti, S.; Miele, E.; De Angelis, F.; Di Fabrizio, E.; Proietti Zaccaria, R.; Capiglia, C. Review on Recent Progress of Nanostructured Anode Materials for Li-Ion Batteries. *J. Power Sources* **2014**, *257*, 421–443.

(6) Marom, R.; Amalraj, S. F.; Leifer, N.; Jacob, D.; Aurbach, D. A Review of Advanced and Practical Lithium Battery Materials.

(7) Kim, A.; Park, E.; Lee, H.; Kim, H. Highly Reversible Insertion of Lithium into MoO2 as an Anode Material for Lithium Ion Battery. *J. Alloys Compd.* **2016**, *681*, 301–306.

(8) Niu, C.; Li, J.; Jin, H.; Shi, H.; Zhu, Y.; Wang, W.; Cao, M. Self-Template Processed Hierarchical V_2O_5 Nanobelts as Cathode for High Performance Lithium Ion Battery. *Electrochim. Acta* **2015**, *182*, 621–628.

(9) Dahn, J. R.; Sacken, U. von; Juzkow, M. W.; Al-Janaby, H. Rechargeable $LiNiO_2$/Carbon Cells. *J. Electrochem. Soc.* **1991**, *138* (8), 2207.

(10) Zhang, Y.; Wang, C.-Y. Cycle-Life Characterization of Automotive Lithium-Ion Batteries with $LiNiO_2$ Cathode. *J. Electrochem. Soc.* **2009**, *156* (7), A527.

(11) Cho, J.; Kim, T.-J.; Kim, Y. J.; Park, B. High-Performance ZrO_2-Coated $LiNiO_2$ Cathode Material. *Electrochem. Solid-State Lett.* **2001**, *4* (10), A159.

(12) Kim, J.-M.; Chung, H.-T. Role of Transition Metals in Layered Li[Ni,Co,Mn]O_2 under Electrochemical Operation. *Electrochim. Acta* **2004**, *49* (21), 3573–3580.

(13) Okada, S.; Sawa, S.; Egashira, M.; Jun-ichi, Y.; Tabuchi, M.; Kageyama, H.; Tokuzo, K.; Yoshino, A. Cathode Properties of Phospho-Olivine $LiMPO_4$ for Lithium Secondary Batteries. *J. Power Sources* **2001**, *97–98*, 430–432.

(14) Martha, S. K.; Grinblat, J.; Haik, O.; Zinigrad, E.; Drezen, T.; Miners, J. H.; Exnar, I.; Kay, A.; Markovsky, B.; Aurbach, D. $LiMn_{0.8}Fe_{0.2}PO_4$: An Advanced Cathode Material for Rechargeable Lithium Batteries. *Angew. Chemie Int. Ed.* **2009**, *48* (45), 8559–8563.

(15) Wu, J.; Byrd, I.; Jin, C.; Li, J.; Chen, H.; Camp, T.; Bujol, R.; Sharma, A.; Zhang, H. Reinvigorating Reverse-Osmosis Membrane Technology to Stabilize the V_2O_5 Lithium-Ion Battery Cathode. *ChemElectroChem* **2017**, *4* (5), 1181–1189.

(16) Ban, C.; Chernova, N. A.; Whittingham, M. S. Electrospun Nano-Vanadium Pentoxide Cathode. *Electrochem. commun.* **2009**, *11* (3), 522–525.

(17) Petkov, V.; Zavalij, P. Y.; Lutta, S.; Whittingham, M. S.; Parvanov, V.; Shastri, S. Structure beyond Bragg: Study of V_2O_5 Nanotubes. *Phys. Rev. B* **2004**, *69* (8), 85410.

(18) Takahashi, K.; Limmer, S. J.; Wang, Y.; Cao, G. Growth and Electrochemical Properties of Single-Crystalline V_2O_5 Nanorod Arrays. *Jpn. J. Appl. Phys.* **2005**, *44* (1B), 662–668.

(19) Zhang, K.-F.; Zhang, G.-Q.; Liu, X.; Su, Z.-X.; Li, H.-L. Large Scale Hydrothermal Synthesis and Electrochemistry of Ammonium Vanadium Bronze Nanobelts. *J. Power Sources* **2006**, *157* (1), 528–532.

(20) Semenenko, D. A.; Itkis, D. M.; Pomerantseva, E. A.; Goodilin, E. A.; Kulova, T. L.; Skundin, A. M.; Tretyakov, Y. D. $LixV_2O_5$ Nanobelts for High Capacity Lithium-Ion Battery Cathodes. *Electrochem. commun.* **2010**, *12* (9), 1154–1157.

(21) Nishi, Y. The Development of Lithium Ion Secondary Batteries. *Chem. Rec.* **2001**, *1* (5), 406–413.

(22) Lian, P.; Zhu, X.; Liang, S.; Li, Z.; Yang, W.; Wang, H. Large Reversible Capacity of High Quality Graphene Sheets as an Anode Material for Lithium-Ion

Batteries. *Electrochim. Acta* **2010**, *55* (12), 3909–3914.

(23) Zhou, G.; Wang, D.-W.; Li, F.; Zhang, L.; Li, N.; Wu, Z.-S.; Wen, L.; Lu, G. Q. (Max); Cheng, H.-M. Graphene-Wrapped Fe_3O_4 Anode Material with Improved Reversible Capacity and Cyclic Stability for Lithium Ion Batteries. *Chem. Mater.* **2010**, *22* (18), 5306–5313.

(24) Liu, Y.; Xue, J. S.; Zheng, T.; Dahn, J. R. Mechanism of Lithium Insertion in Hard Carbons Prepared by Pyrolysis of Epoxy Resins. *Carbon N. Y.* **1996**, *34* (2), 193–200.

(25) Buiel, E.; Dahn, J. R. Li-Insertion in Hard Carbon Anode Materials for Li-Ion Batteries. *Electrochim. Acta* **1999**, *45* (1), 121–130.

(26) Zheng, T.; Liu, Y.; Fuller, E. W.; Tseng, S.; Sacken, U. von; Dahn, J. R. Lithium Insertion in High Capacity Carbonaceous Materials. *J. Electrochem. Soc.* **1995**, *142* (8), 2581.

(27) Noel, M.; Suryanarayanan, V. Role of Carbon Host Lattices in Li-Ion Intercalation/de-Intercalation Processes. *J. Power Sources* **2002**, *111* (2), 193–209.

(28) Xing, W.; Xue, J. S.; Dahn, J. R. Optimizing Pyrolysis of Sugar Carbons for Use as Anode Materials in Lithium-Ion Batteries. *J. Electrochem. Soc.* **1996**, *143* (10), 3046–3052.

(29) Väli, R.; Jänes, A.; Thomberg, T.; Lust, E. Synthesis and Characterization of D-Glucose Derived Nanospheric Hard Carbon Negative Electrodes for Lithium- and Sodium-Ion Batteries. *Electrochim. Acta* **2017**, *253*, 536–544.

(30) Simone, V.; Boulineau, A.; de Geyer, A.; Rouchon, D.; Simonin, L.; Martinet, S. Hard Carbon Derived from Cellulose as Anode for Sodium Ion Batteries: Dependence of Electrochemical Properties on Structure. *J. Energy Chem.* **2016**, *25* (5), 761–768.

(31) Ni, J.; Huang, Y.; Gao, L. A High-Performance Hard Carbon for Li-Ion Batteries and Supercapacitors Application. *J. Power Sources* **2013**, *223*, 306–311.

(32) Dahn, J. R.; Zheng, T.; Liu, Y.; Xue, J. S. Mechanism for Lithium Insertion in Carbonaceous Materials. *Science (80-.).* **1995**, *270* (5236), 590.

(33) Lee, S.-J.; Nishizawa, M.; Uchida, I. Fabrication of Mesophase Pitch Carbon Thin Film Electrodes and the Effect of Heat Treatment on Electrochemical Lithium Insertion and Extraction. *Electrochim. Acta* **1999**, *44* (14), 2379–2383.

(34) Peled, E.; Eshkenazi, V.; Rosenberg, Y. Study of Lithium Insertion in Hard Carbon Made from Cotton Wool. *J. Power Sources* **1998**, *76* (2), 153–158.

(35) Hu, J.; Li, H.; Huang, X. Electrochemical Behavior and Microstructure Variation of Hard Carbon Nano-Spherules as Anode Material for Li-Ion Batteries. *Solid State Ionics* **2007**, *178* (3–4), 265–271.

(36) Yi, J.; Li, X. P.; Hu, S. J.; Li, W. S.; Zhou, L.; Xu, M. Q.; Lei, J. F.; Hao, L. S. Preparation of Hierarchical Porous Carbon and Its Rate Performance as Anode of Lithium Ion Battery. *J. Power Sources* **2011**, *196* (16), 6670–6675.

(37) Yang, J.; Zhou, X. Y.; Li, J.; Zou, Y. L.; Tang, J. J. Study of Nano-Porous Hard Carbons as Anode Materials for Lithium Ion Batteries. *Mater. Chem. Phys.* **2012**, *135* (2–3), 445–450.

(38) Sheem, K.-Y.; Song, E.-H.; Lee, Y. H. High-Rate Charging Performance Using High-Capacity Carbon Nanofilms Coated on Alumina Nanoparticles for Lithium Ion Battery Anode. *Electrochim. Acta* **2012**, *78*, 223–228.

(39) Jache, B.; Neumann, C.; Becker, J.; Smarsly, B. M.; Adelhelm, P. Towards Commercial Products by Nanocasting: Characterization and Lithium Insertion Properties of Carbons with a Macroporous, Interconnected Pore Structure. *J. Mater. Chem.* **2012**, *22* (21), 10787.

(40) Chang, J.-C.; Tzeng, Y.-F.; Chen, J.-M.; Chiu, H.-T.; Lee, C.-Y. Carbon Nanobeads as an Anode Material on High Rate Capability Lithium Ion Batteries. *Electrochim. Acta* **2009**, *54* (27), 7066–7070.

(41) Xing, W.; Dahn, J. R. Study of Irreversible Capacities for Li Insertion in Hard and Graphitic Carbons. *J. Electrochem. Soc.* **1997**, *144* (4), 1195–1201.

(42) Buiel, E.; Dahn, J. R. Reduction of the Irreversible Capacity in Hard-Carbon Anode Materials Prepared from Sucrose for Li-Ion Batteries. *J. Electrochem. Soc.* **1998**, *145* (6), 1977–1981.

(43) Buiel, E. Lithium Insertion In Hard Carbon Anode Materials For Li-Ion Batteries.

J. Electrochem. Soc. **1998**, *145* (4), 1179–1183.

(44) Kim, K. J.; Lee, T. S.; Kim, H. G.; Lim, S. H.; Lee, S. M. A Hard Carbon/microcrystalline Graphite/carbon Composite with a Core-Shell Structure as Novel Anode Materials for Lithium-Ion Batteries. *Electrochim. Acta* **2014**, *135*, 27–34.

(45) Jiang, J.; Zhu, J.; Ai, W.; Fan, Z.; Shen, X.; Zou, C.; Liu, J.; Zhang, H.; Yu, T. Evolution of Disposable Bamboo Chopsticks into Uniform Carbon Fibers: A Smart Strategy to Fabricate Sustainable Anodes for Li-Ion Batteries. *Energy Environ. Sci.* **2014**, *7* (8), 2670–2679.

(46) Lotfabad, E. M.; Ding, J.; Cui, K.; Kohandehghan, A.; Kalisvaart, W. P.; Hazelton, M.; Mitlin, D. High-Density Sodium and Lithium Ion Battery Anodes from Banana Peels. *ACS Nano* **2014**, *8* (7), 7115–7129.

(47) Lv, W.; Wen, F.; Xiang, J.; Zhao, J.; Li, L.; Wang, L.; Liu, Z.; Tian, Y. Peanut Shell Derived Hard Carbon as Ultralong Cycling Anodes for Lithium and Sodium Batteries. *Electrochim. Acta* **2015**, *176*, 533–541.

(48) Wang, Q.; Li, H.; Chen, L.; Huang, X. Monodispersed Hard Carbon Spherules with Uniform Nanopores. *Carbon N. Y.* **2001**, *39* (14), 2211–2214.

(49) Wang, Q.; Li, H.; Chen, L.; Huang, X. Novel Spherical Microporous Carbon as Anode Material for Li-Ion Batteries. *Solid State Ionics* **2002**, *152–153*, 43–50.

(50) Hu, J.; Li, H.; Huang, X. Influence of Micropore Structure on Li-Storage Capacity in Hard Carbon Spherules. *Solid State Ionics* **2005**, *176* (11–12), 1151–1159.

(51) Huo, K.; An, W.; Fu, J.; Gao, B.; Wang, L.; Peng, X.; Cheng, G. J.; Chu, P. K. Mesoporous Nitrogen-Doped Carbon Hollow Spheres as High-Performance Anodes for Lithium-Ion Batteries. *J. Power Source* **2016**, *324*, 233–238.

(52) Dong, W.; Xu, J.; Wang, C.; Lu, Y.; Liu, X.; Wang, X.; Yuan, X.; Wang, Z.; Lin, T.; Sui, M.; et al. A Robust and Conductive Black Tin Oxide Nanostructure Makes Efficient Lithium-Ion Batteries Possible. *Adv. Mater.* **2017**, *29* (24), 1–9.

(53) Mohamedi, M.; Lee, S.-J.; Takahashi, D.; Nishizawa, M.; Itoh, T.; Uchida, I. Amorphous Tin Oxide Films: Preparation and Characterization as an Anode Active Material for Lithium Ion Batteries. *Electrochim. Acta* **2001**, *46* (8), 1161–

1168.

(54) Guo, B.; Shu, J.; Tang, K.; Bai, Y.; Wang, Z.; Chen, L. Nano-Sn/hard Carbon Composite Anode Material with High-Initial Coulombic Efficiency. *J. Power Sources* **2008**, *177* (1), 205–210.

(55) Meduri, P.; Pendyala, C.; Kumar, V.; Sumanasekera, G. U.; Sunkara, M. K. Hybrid Tin Oxide Nanowires as Stable and High Capacity Anodes for Li-Ion Batteries. *Nano Lett.* **2009**, *9* (2), 612–616.

(56) Han, S.; Jang, B.; Kim, T.; Oh, S. M.; Hyeon, T. Simple Synthesis of Hollow Tin Dioxide Microspheres and Their Application to Lithium-Ion Battery Anodes. *Adv. Funct. Mater.* **2005**, *15* (11), 1845–1850.

(57) Liu, J.; Li, W.; Manthiram, A. Dense Core-Shell Structured SnO2/C Composites as High Performance Anodes for Lithium Ion Batteries. *Chem. Commun. (Camb).* **2010**, *46* (9), 1437–1439.

(58) Lou, X. W.; Deng, D.; Lee, J. Y.; Archer, L. A. Preparation of SnO_2 /Carbon Composite Hollow Spheres and Their Lithium Storage Properties. *Chem. Mater.* **2008**, *20* (20), 6562–6566.

(59) Lou, X. W.; Li, C. M.; Archer, L. A. Designed Synthesis of Coaxial SnO2@carbon Hollow Nanospheres for Highly Reversible Lithium Storage. *Adv. Mater.* **2009**, *21* (24), 2536–2539.

(60) Huang, B.; Li, X.; Pei, Y.; Li, S.; Cao, X.; Massé, R. C.; Cao, G. Novel Carbon-Encapsulated Porous SnO_2 Anode for Lithium-Ion Batteries with Much Improved Cyclic Stability. *Small* **2016**, *12* (14), 1945–1955.

(61) Zhao, K.; Zhang, L.; Xia, R.; Dong, Y.; Xu, W.; Niu, C.; He, L.; Yan, M.; Qu, L.; Mai, L. SnO_2 Quantum Dots@Graphene Oxide as a High-Rate and Long-Life Anode Material for Lithium-Ion Batteries. *Small* **2016**, *12* (5), 588–594.

(62) Hou, K.; Wen, X.; Yan, P.; Tang, A.; Yang, H. Tin Oxide-Carbon-Coated Sepiolite Nanofibers with Enhanced Lithium-Ion Storage Property. *Nanoscale Res. Lett.* **2017**, *12* (1), 215.

(63) Winter, M.; Besenhard, J. O.; Spahr, M. E.; Novák, P. Insertion Electrode Materials for Rechargeable Lithium Batteries. *Adv. Mater.* **1998**, *10* (10), 725–763.